

CZECH TECHNICAL UNIVERSITY IN PRAGUE

Faculty of Mechanical Engineering

Department of Automotive, Combustion Engine and Railway
Engineering

Study program: Master of Automotive Engineering

Field of study: Advanced Powertrains



MIXTURE HOMOGENEITY EVALUATION FOR CNG PORT FUEL INJECTION

Author	: Shubham Bawkar
Supervisor	: Ing. Jiří Vávra, Ph.D.
Tutor's	: Doc. Ing. Oldrich Vitek, Ph.D. : Ing. Vít Doleček, Ph.D.
Year	: 2020

Disclaimer

I hereby declare that the following thesis is my independent work and to the best of knowledge. I have only used the document listed in the attachments. It contains no materials previously published or written by any other person.

In Prague :15/08/2020

Shubham Bawkar.

Acknowledgment

First, I would like to express my sincere gratitude to my thesis supervisor Ing. Jiří Vávra, Ph.D. for giving me this opportunity. His guidance, continuous support, knowledge has motivated me throughout my thesis and helped me achieve my goals. Besides my supervisor, I am grateful to Ing. Vít Doleček, Ph.D. & special thanks to Doc. Ing. Oldrich Vitek, Ph.D. for their consultations & for all the help in the software AVL FIRE. And finally, I would like to thank my family and friends for all the love, support, and care throughout my studies.

Shubham Bawkar.

Abstract

This thesis deals with the conversion of a four-cylinder, 4-stroke diesel engine into a spark ignited CNG engine, design, and assembly of a port fuel injection system for methane injection into individual air inlet ports per cylinder & evaluating the mixture homogeneity of the port fuel injection system. Initially, the mass flow rate of methane was calculated to achieve the rated engine operating conditions and then a market survey for OEM parts was carried out. Base on the survey and OEM parts that could be used to satisfy the fuel mass flow rates, the design of the injection location, the assembly of different parts & preparation of manufacturing drawings of all the designed parts was done using 3D CAD software PTC Creo. Later on, simulations were performed on the designed fuel injection location using the software AVL FIRE for the evaluation of the mixing homogeneity for the port fuel injection system.

Keywords: *CNG, Methane injection, Mixture homogeneity, Port fuel injection, Mass flow rate.*

Table of Content

Nomenclature.....	2
1 Introduction	4
1.1 Current issues in the transportation sector.....	4
1.2 Natural gas as an alternative fuel.....	5
1.3 Research motivation & scope of the thesis.....	6
2 Literature Review.....	7
2.1 Lean burn combustion.....	7
2.2 Pre-Chamber combustion.....	9
3 3-D CAD & Experimental Setup.....	14
3.1 Experimental engine.....	14
3.2 CNG common rail selection for desired engine operating condition.....	15
3.3 CNG gas supply to the Landi Renzo Evo common rail.....	17
4 Matching the Engine with Common Rail.....	18
4.1 Manifold insert fuel exit velocity.....	19
4.2 Mass flow rate sensitivity analysis for one engine cycle.....	25
5 Part Design	27
5.1 Intake manifold details.....	28
5.2 Holder details.....	30
5.3 Assembly details	31
5.4 Purchased parts	33
5.4.1 Flexible gas hose.....	34
5.4.2 Hose clamps.....	34
5.4.3 Tee split.....	35
6 AVL FIRE Simulation.....	36
6.1 Simulation Case Setup & Boundary Conditions.....	41
6.2 Simulation Results.....	44
7 Summary & Conclusion	53
8 Thesis Contribution & Future Research Scope.....	56
9 References.....	57
List of Figure	59
List of Tables.....	61
List of Files in Attached CD	62
Attachments.....	63

Nomenclature

ΔU	Change in internal energy
\dot{m}_{fuel}	Mass Flow Rate of Fuel
μ_T	Eddy Viscosity
τ_{ij}	Reynolds Stress Tensor
\bar{A}	Time Averaged Turbulent Quantity
A'	Turbulent Fluctuating Part
S_{ij}	Mean Strain Tensor
1D	One Dimensional
2D	Two Dimensional
3D	Three Dimensional
BDC	Bottom Dead Center
BP	Brake Power
BSFC	Brake Specific Fuel Consumption
CH ₄	Methane
CNG	Compressed Natural Gas
CO	Carbon Monoxide
CO ₂	Carbon Dioxide
c_p	Specific Heat Capacity
CR	Common Rail
$D \cdot n$	Normal Component of Deformation Tensor
EOI	End of Injection
GHG	Greenhouse Gas
ICE	Internal Combustion Engine
LNG	Liquefied Natural Gas
MEP	Mean Effective Pressure
NO	Nitric Monoxide
NO ₂	Nitrogen Dioxide
NO _x	Oxides of Nitrogen
P	Actual Pressure of The Gas
r_c	Compression Ratio
RPM	Revolutions Per Minute
SI	Spark Ignition
SOI	Start of Injection

$T \cdot n$	Normal Component of the Stress Tensor
TDC	Top Dead Center
$u \cdot n$	Normal Component of Velocity
UHC	Unburnt Hydrocarbon
γ	Specific Heat Ratio
ϵ	Dissipation per Unit Mass
η	Indicated Thermal Efficiency
λ	Air Excess (lambda)
μ	Dynamic Viscosity
ν	Kinematic Viscosity

1 Introduction

Transportation is a crucial component of all efforts to reduce air pollution, as vehicles are a major source of air pollution all around the world. Although we have made great efforts in cleaning up automotive emissions, we are also driving more. Air pollution is caused by the emission of small particles or noxious gases being released into the atmosphere, from the exhaust of the automobiles. These gases include carbon monoxide, sulfur dioxide, nitrogen oxide, and chemical vapors to name a few. The gases also can cause a chain-reaction event that results in the atmospheric phenomenon which has acid precipitation and smog. If left unchecked, the chemical aspect of pollution could become the most important contributor to premature death within the world, above the speed of cancer, automobile accidents, or any other cause of unnatural or premature death. [1]

1.1 Current issues in the transportation sector.

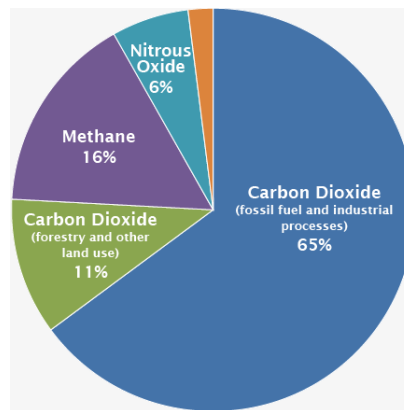


Figure 1.1:1 Global Greenhouse Gas Emissions [2]

Greenhouse gas emissions from the transportation sector primarily involve fossil fuels burned for road, rail, air, and marine transportation. Almost (95%) of the world's transportation energy comes from petroleum-based fuels, largely gasoline and diesel [2]. Even though automobiles have a certain advantage, consumption of non-renewable resources and pollution have to be addressed as the major drawback of this sector. From the recent research and data acquired on emission the Figure 1.1:1 (above) shows the effect of greenhouse gas emission on a global scale, even though CO_2 & H_2O (which later turns to water vapor) are the product of perfect combustion they remain to be the most dominant source of greenhouse gas emission. Due to incomplete combustion of gasoline or diesel gases like carbon monoxide, unburnt hydrocarbons contribute to the increase in GHG. Oxides of nitrogen when inhaled in an excessive amount cause severe respiratory problems in individuals. As addressed in the

above-mentioned issues, few of the challenges faced by the automotive manufactures are to build an ICE (internal combustion engine) with an improved efficiency adhering to the strict emission norms [3], building cost-effective catalytic converters for exhaust gas after-treatment & reducing the overall cost to make their products competitive in the market.

1.2 Natural gas as an alternative fuel.

Natural gas has been used as fuel for transportation for many years and, currently, about half a million vehicles of various types are running either on compressed gas (CNG) or on liquefied natural gas (LNG). Natural gas is composed essentially of methane, which can be obtained through anaerobic fermentation of different organic products that produce biogas (60% methane).

The importance of methane as a fuel has increased its importance due to the growth in digester construction all over the world. The main advantages of Natural gas which include both CNG & LPG are its low pollutant exhaust emissions, high-octane ratings, and relatively low cost as compared to gasoline & diesel. However, due to its low-cetane number, it might not perform satisfactorily in diesel engines [4] [5] [6].

Natural gas has a high-octane number, this signifies that natural gases are more resistant to knock. As they are more resistant to knock, they can be used in engines with higher compression ratios than conventional SI engines. Hence, natural gas can achieve higher thermal efficiency than the conventional fuels when used in a SI engine [7].

When operated in a lean air-fuel mixture, natural gas offers various advantages [7]. Due to lower in-cylinder temperature, as compared to $\lambda=1$ operation, the production of NO_x is reduced to a considerable amount. Natural gas is usually promoted as a clean source of fuel and consumers have to pay lower taxes which then reduces the cost per kilometer. Also, natural gas is present in the world with quite a higher amount than crude oil. The most important fact is that the development of already existing engines into a bi-fuel configuration is not expensive as well as the development of brand new CNG engine is distinctly cheaper than the development of an electric car.

1.3 Research motivation & scope of the thesis

The most challenging task faced by the automotive manufacturers all around the globe is to decrease the emission for their cars to avoid high legislative penalties, natural gas can be used as an alternative fuel to satisfy legislative norms as well as offer a good deal for customers by lower costs per kilometer. The technical advantage of using natural gas is that when burnt at a lean mixture it decreases the amount of CO due to a higher amount of air present to burn the fuel and freeze's the chemistry of NOx formation due to lower temperature of the flame [8]. It has a high octane number around 130, which decreases the probability of knocking and increase the power of the engine [6] [7].

The primary goal of this thesis is to convert an existing diesel engine into a SI gas engine. The thesis describes design changes made and component selection for the conversion as mentioned above and ports fuel injection control strategy for methane as fuel. The design part deals with the simplification and modularity of the product by using mass-produced parts and optimization of the space coupled with the injection strategy to be used.

The secondary goal of this thesis is to create and test a 3-D CFD model of an intake stroke with a predefined intake valve lift which gives a better understanding of air-fuel mixture development processes starting at the point of port injected fuel and continuing for the entire intake stroke in the cylinder. The model focuses on evaluating the mixture homogeneity of air & methane during an intake stroke. The CFD model is configured based on the data from a 1-D model created on GT – Suite by one of our colleagues. In this stage, the 3-D CFD model does not include the combustion process. The 3- D CFD model only considers the steady-state simulations as this is the initial conversion stage of the engine. A transient simulation would give a more accurate result but that is not in the scope of this thesis.

Details of the thesis task are as follows.

- 1) Selection of appropriate components for a CNG port fuel injection.
- 2) Design and implementation of the selected components into the engine layout.
- 3) Prepare manufacturing drawings of the design.
- 4) Using CFD evaluate mixture homogeneity for the design for selected operating points and selected injection control strategy.
- 5) Suggest the means for mixture homogeneity optimization.

2 Literature Review

As automotive manufactures are constantly battling to reduce their engine emission, from the above discussion it seems appropriate to switch to natural gas to keep the magnitude of emission with legislative limits and still have competitive products in the market. To achieve a solution for the above-mentioned problem, the lean-burn combustion concept is used which limits the in-cylinder temperatures and avoids NO_x formation. The advantage of lean-burn combustion is that the low emission requirements are met, on the other hand, such an approach requires high flame speed to achieve rapid combustion which is a bit difficult in lean-burn combustion. But the solution for lower flame speed due to lean burning can be solved by using indirect injection methods like pre-chamber ignition also referred to as jet ignition [5] [9] [10] which are discussed below.

2.1 Lean burn combustion.

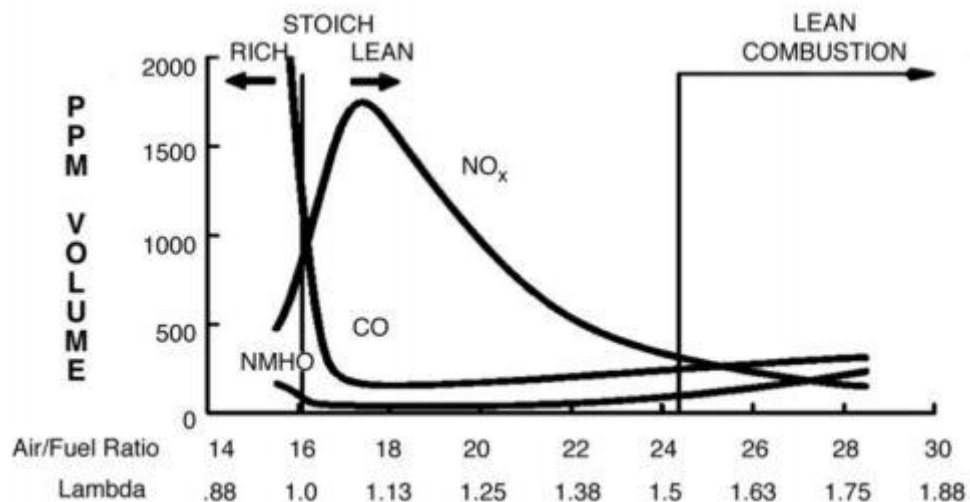


Figure 2.1:1 Emission versus air/fuel ratio [9].

To understand lean burn combustion, we should first get acquainted with few terms like stoichiometric air-fuel ratio & air excess (lambda). The stoichiometric air-fuel ratio is defined as the amount of air (by mass) required to burn 100 % fuel (by mass) which consumes all the available oxygen from the incoming air, for example, the stoichiometric air-fuel ratio is 16: 1. This means that 16 kg of air is required for complete combustion of 1 kg of fuel. Whereas the air excess (lambda) is defined as the ratio of actual air-fuel ratio to the stoichiometric air-fuel ratio. By actual air-fuel ratio, we mean the air-fuel ratio at which the engine is operating under normal working conditions [8].

$$\lambda = \frac{\text{air/fuel ratio (actual)}}{\text{air/fuel ratio (stoichiometric)}}$$

Eq 1

Now from the above equation it is clear that lean burn occurs when the air/fuel (A/F) ratio or lambda is greater than 1 i.e., additional air is added to the mixture when compared to the stoichiometric A/F ratio [8] [11]. The pollutants entering the atmosphere from the incomplete combustion can be measured by the main emissions of Carbon Monoxide (CO), Hydrocarbon gas (HC), and Nitrogen Oxide (NO_x). Figure 2.1:1 (above) shows the graphical representation of the emissions in parts per million (ppm) versus the A/F ratio, it can be noticed that running the engine on a lean A/F mixture results in decreased emissions. This happens because enough air is available to burn all the fuel which means there will be no products from incomplete combustion. However, irrespective of the mixture is rich or lean some amount of A/F mixture gets trapped in the crevices of the compression rings & oil rings which does not burn which is processed in the catalytic converter [8]. Under cold-start or generally under cold conditions, some of the other HC sources such as lubricating oil films, and single-wall flame quenching are believed to become equally important with combustion-chamber crevices [8] [12] which can be seen in Figure 2.1:2 (below). The combustion of the air-fuel mixture is fast, but not instantaneous, resulting in the production of heat and pollutant gases. Lean burn combustion helps to reduce both the in-cylinder temperature as well as pollutants like NO_x. The NO_x formation takes place at very high in-cylinder temperatures, lean burn combustion reduces the in-cylinder which results in a decrease of NO_x formation. Also, due to excess oxygen, the combustion process is more efficient, and more energy is generated from the same amount of fuel [11].

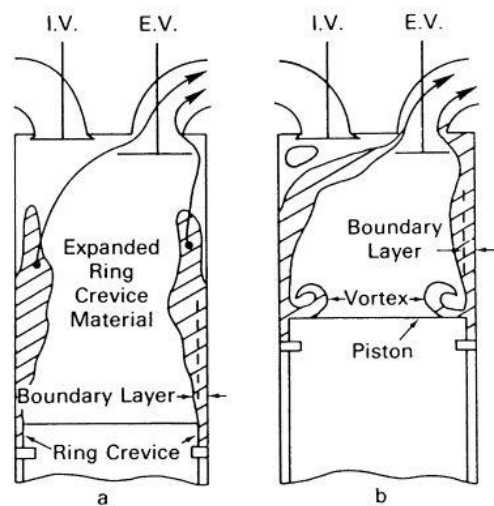


Figure 2.1:2 Schematic of flow processes by which piston crevice HC exit the cylinder: (a) exhaust blowdown process; (b) during exhaust stroke [12].

Additional air in the lean mixture increases the specific heat ratio which results in increased thermal efficiency.

$$\eta = \frac{1}{r_c^{(\gamma-1)}} \quad \text{Eq 2}$$

Where:

η = Indicated thermal efficiency

r_c = Compression ratio

γ = Specific Heat Ratio

Even though with all the above-mentioned advantages, there are few limitations in using a lean mixture. The primary disadvantage of this method is it results in low flame speeds and in actual operating conditions flame speed required to combust the A/F mixture is high. If the flame speed is too low it might result in a misfire which in turn will result in high unburnt hydrocarbon (UHC) emissions. Therefore, the lean burn limit is restricted by the capability of the ignition system to ignite the A/F mixture. To overcome the above limitation alternative ignition system should be considered. This can be achieved by using any of the following methods - creating high turbulence, turbocharging, and using advanced combustion techniques [9].

2.2 Pre-Chamber combustion.

One of the most appealing solutions to the lean-burn combustion limitation is the pre-chamber combustion method, sometimes also referred to as indirect ignition system. This innovative combustion concept was developed & patented in 1918 by Sir Harry Ricardo [13]. This type of system consists of a small chamber (pre-chamber) which is connected to the main combustion chamber. The pre-chamber constitutes approximately 2% of the total compression volume and has its own supply of fuel. The spark plug is placed in the pre-chamber. Figure 2.2:1 (below) shows the cross-section diagram of the pre-chamber combustion and position of the components.

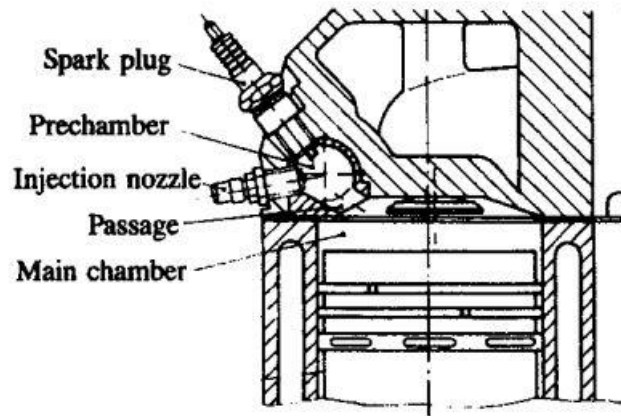


Figure 2.2:1 Cross-section of a typical Pre-Chamber Combustion System [8].

Recently, Mahle powertrains have developed & patented a pre-chamber combustion ignition system called the Turbulent Jet Ignition (TJI) system. This system consists of the main chamber along with a small pre-chamber and two separate injectors which supply fuel to the main combustion chamber and pre-chamber. The spark plugs and one of the injectors are placed in the pre-chamber casing. The fuel is supplied to the pre-chamber by one of the injectors which is ignited by the spark plug and then the partially combusted fuel is forced through the orifices of the pre-chamber into the main chamber, burning the main chamber charge. To understand the working of the Turbulent Jet Ignition system let us take a look at Figure 2.2:2 (below) which shows the cross-section of Mahle powertrains TJI.

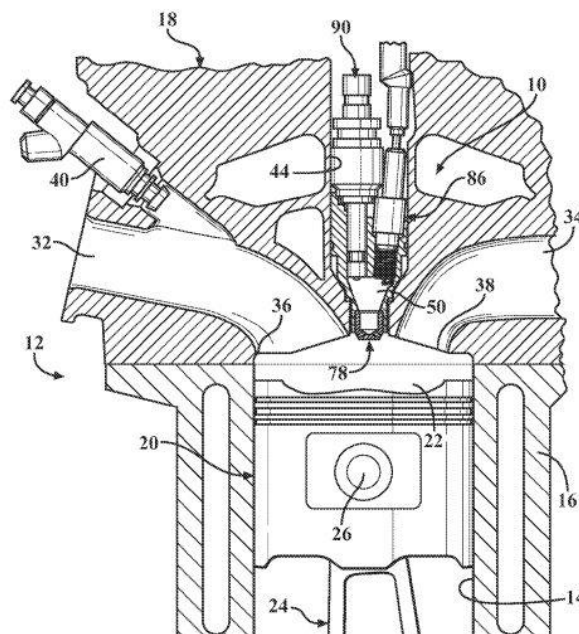


Figure 2.2:2 Partial cross-section of Mahle Powertrain TJI system [14].

This experimental engine which is used by Mahle and is a single-cylinder engine with four valves. The compression ratio of the engine is 10.4 and peak indicated net thermal efficiency is 42 % with almost zero NO_x emissions [15]. Overall swept volume is 0.6 dm³, the pre-chamber consists of 6 holes each with a length of 3 mm & diameter of 1.25 mm. The primary injector (40) is a standard gasoline port fuel injector that injects 98 % of fuel in the intake manifold (32). The secondary injector (90) provides the remaining 2 % of fuel in the pre-chamber where the slightly rich mixture is maintained whereas, the mixture in the main combustion chamber (22) is lean. During the compression stroke, as the piston (20) moves upwards from the bottom dead center (BDC) towards the top dead center (TDC) the volume of the cylinder starts to decrease thus compressing the air-fuel mixture, raising its pressure and temperature. As the piston continues to travel upward along with the inlet and exhaust valves closed the lean mixture having nowhere to go starts to move into the pre-chamber (50) through the 6 holes where its pressure and temperature are further raised until the piston reaches the TDC. Remaining 2% of the fuel is sprayed by the secondary injector (90) into the pre-chamber and the mixture now is slightly rich than the mixture present in the main chamber (22).

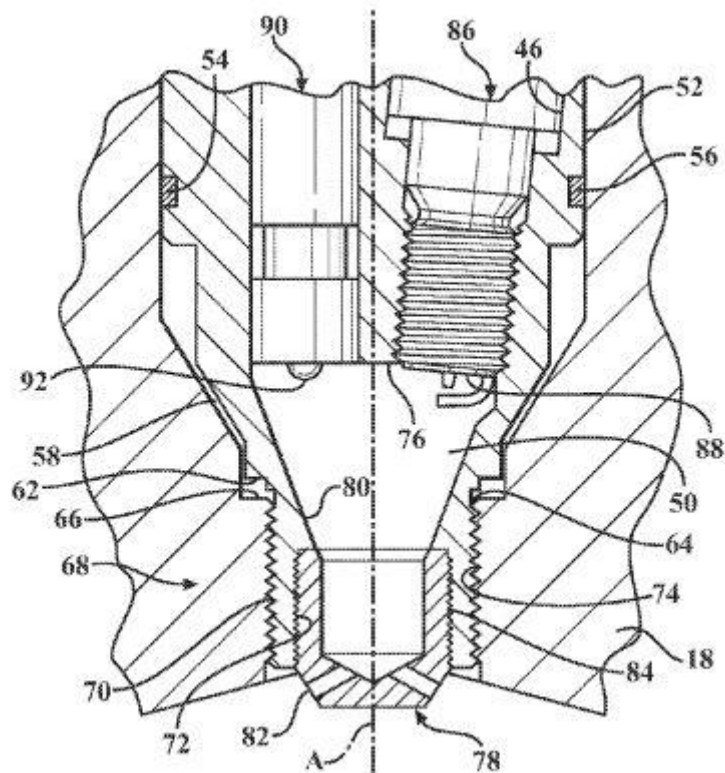


Figure 2.2:3 Detailed cross-section of Mahle Powertrain TJI system [14].

As the piston is about to reach TDC, few degrees before TDC a spark is created by the spark plug (86) and a stable flame kernel is established near the spark plug gap (88) which burns the mixture inside the pre-chamber (50) extremely fast further raising its pressure and

temperature. Now, as the pressure inside the pre-chamber (50) is higher than the pressure in the main combustion chamber (22), the partially burned mixture rushes out of the hole (82) into the main chamber (22) in the form of a turbulent jet which then ignites the lean mixture in the main combustion chamber completing the combustion stroke. Even though the mixture in the pre-chamber is slightly rich and at a higher temperature the chances of knocking are quite low as there is less time available for auto-ignition of the end charge in the pre-chamber due to its small volume. This arrangement also allows us to have higher compression ratios for the same engines as the mixture in the main chamber is lean. As the flame is highly turbulent the lean mixture in the main chamber also burns at a faster rate at a lower temperature (as the mixture is leaner than the mixture available in the pre-chamber) reducing the chances of the unburnt mixture to be left at the end of combustion stroke reducing the emission of UHC & NO_x. All of these together gives a 30 % lower fuel consumption as compared to the conventional spark-ignition engine [15].

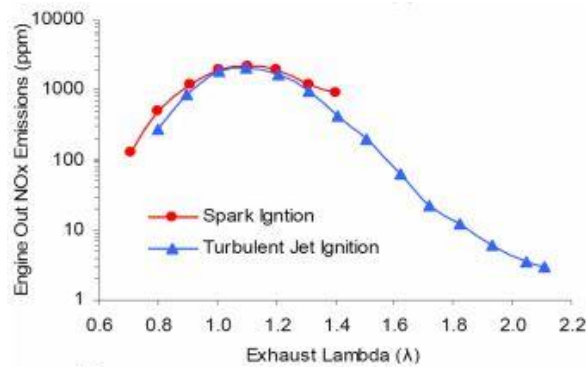


Figure 2.2:4 NO_x comparison of TJI and conventional SI engine [15].

The main advantage of this ignition system is that it can work with a very lean mixture of up to a λ value of 2 as compared to a typical spark-ignition engine that operates up to a λ value of 1.6. In Figure 2.2:4 (above) we can see the difference of NO_x emissions between common spark ignition engine and pre-chamber TJI engine [14] [15].

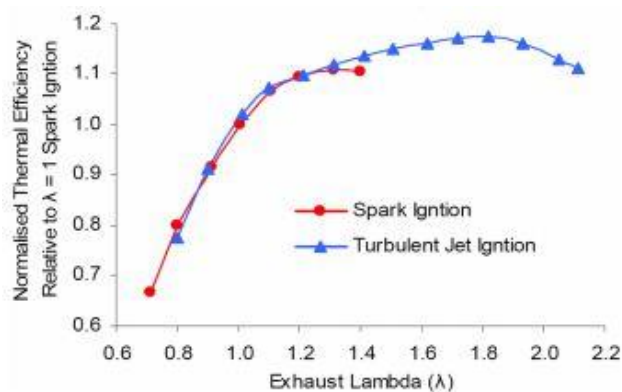


Figure 2.2:5 Normalised thermal efficiency comparison of TJI and conventional SI engine [15].

In Figure 2.2:5 (above) we can see the difference in the normalized thermal efficiencies between the common spark-ignition engine and the pre-chamber TJI engine. Due to lower fuel consumption and higher compression ratio possibility higher thermal efficiencies can be obtained by pre-chamber TJI engines. However, a too lean mixture results in a decrease in thermal efficiency even with a TJI system. As the mixture becomes excessively lean, there is a high chance of misfiring which will cause the air-fuel mixture to leave the cylinder unburnt. Also, having higher lambda results in slow-burning thus reducing the flame propagation speed through the combustion chamber which then cannot burn all the air-fuel mixture inside the combustion chamber and as the exhaust valve opens the unburnt mixture leaves the cylinder into the exhaust port. Hence the available energy in the air-fuel mixture which leaves the cylinder cannot be used which causes a decrease in the thermal efficiency [14] [15].

3 3-D CAD & Experimental Setup

The 3-D CAD model and 2-D drafting drawings are created using the CAD tool PTC Creo. This section refers to the documentation & drawings in the attachment outside the thesis. Initially, there are several prerequisites which the project has to conform to. The main constraint is that the experimental engine is a working diesel engine provided by the Zetor company which needs to be rebuilt as a spark ignited CNG engine. This means that all the necessary parts for the change over from diesel engine to CNG engine must be designed in such a way that less modification should be made to the existing engine and all the designed/selected parts should fit in the given space with minimum changes. The most important module of all was the common rail system for CNG supply to the engine which consists of the pressure regulator, common rail & injectors had to be selected in such a way that the desired power output must be achieved during operation. The common rail has to be mounted in the central position of the intake manifold with no extra adjustments. After some basic fuel flow requirement calculations, it was decided that the common rail provided by Autogas Centrum Plus s.r.o. who provided us with the Landi Renzo system that suits the requirements and can be used. An extremely important parameter was to provide symmetric distribution of gas into the intake ports, as the existing engine has two intake ports per cylinder it was decided to split the flow using a tee split so that fuel can be injected in both the intake ports individually per cylinder. This feature should provide better air-fuel mixing as the fuel is injected at multiple points and sufficient time is available for mixing from the start of injection of fuel to start of combustion. This injection strategy is known as a multipoint fuel injection system (MPFI).

3.1 Experimental engine

The experimental setup was located in Czech Technical University Lab in Josef Bozek Research Centre for Vehicles of Sustainable Mobility. All the modifications to the engine were made in-house. The engine used in the setup is a 4-cylinder 4 stroke tractor diesel engine which will be rebuilt as a SI gas engine. The engine has a bore diameter of 105 mm and a stroke of 120 mm. The displacement volume of the engine is 4156 cm³. The engine is turbocharged with an intercooler and has a compression ratio of 14. The main engine parameter of the original diesel engine arrangement is listed in Table 3.1-1 (below)

No. of cylinder	4
Bore	105 mm
Stroke	120 mm
Displacement Volume	4156 cm ³
Maximum Power	100 kW @ 2200 RPM.
Maximum Torque	570 Nm @ 1480 RPM.
Engine Design	In-line, vertical, water-cooled.
Engine Kind	Diesel 4-stroke, Turbocharged with Intercooler.

Table 3.1-1 Main parameter of the original engine arrangement

3.2 CNG common rail selection for desired engine operating condition.

During the thesis task assignment, it was decided that the rebuilt SI gas engine from the original diesel engine must be operated at the maximum power of 100 kW @ 2200 RPM with brake thermal efficiency of about 40 % (or above is expected) [16]. At the above-mentioned conditions, the brake specific fuel consumption was calculated to be 180 g. kW⁻¹.h⁻¹. Hence to fulfill these requirements, the mass flow rate of fuel was calculated using the following equation.

$$\dot{m}_{fuel} = BSFC * BP \quad Eq 3$$

The mass flow rate of fuel (\dot{m}_{fuel}) calculated from the above-mentioned equation to get the desired operating point was 18 kg.h⁻¹. A CNG common rail kit provided by Landi Renzo company was decided to be used having the parameters for common rail & pressure regulator listed in Table 3.2-1 (below).

Common Rail Kit	Landi Renzo EVO
Injector Type	Normally Closed
Working Temperature	-40 °C to 120 °C
Working Pressure (Absolute)	1.5 bars to 5 bars
Class IP	IP 54

Table 3.2-1 Landi Renzo Evo Common Rail & Injector Parameters.



Figure 3.2:1 Landi Renzo Evo Common Rail & Injectors

Table 3.2-1 (above) shows the image of the Landi Renzo Evo common rail & injectors. Pressure regulator parameters are listed in Table 3.2-2 (below) and Figure 3.2:2 (below) shows the image of the Landi Renzo Evo pressure regulator.

Pressure Regulator	Landi Renzo EVO
Pressure Regulator Model	NG - 1
Operating Pressure (Absolute)	3 bars
Safety Valve Pressure Setting (Absolute)	4.5 bars
Nominal Operating Mass Flow Rate of Fuel	25 kg.h ⁻¹

Table 3.2-2 Landi Renzo Evo Pressure Regulator Parameters.



Figure 3.2:2 Landi Renzo Evo NG-1 Pressure Regulator

3.3 CNG gas supply to the Landi Renzo Evo common rail.

The fuel is supplied to the common rail by the CNG gas line in the laboratory with the pressure of up to 200 bar in the line. The pressure from the gas line is controlled by the pressure regulator shown in Figure 3.2:2 (above). Fuel flow to the CR is controlled by the pressure regulator and measured by a Coriolis flow meter. The fuel then enters the common rail which then supplies the required amount of fuel mass flow rate to intake ports. All pressures mentioned in Figure 3.3:1 (below) are absolute pressures.

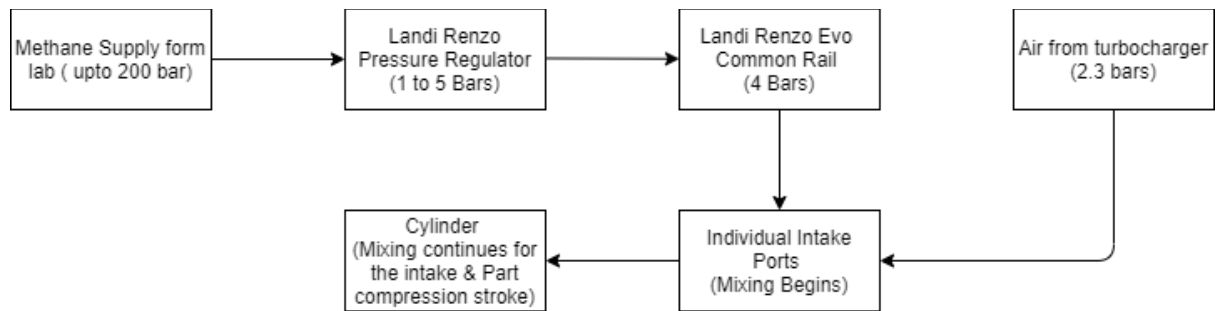


Figure 3.3:1 Schematic diagram for the CNG gas supply to the Landi Renzo Evo common rail.

4 Matching the Engine with Common Rail.

As the most important part that will control the engine output, matching the common rail to the engine to achieve precise metering of fuel was extremely important. In order to do so, analytical models of the basic conservation laws were used. The most significant task was to set the correct actual mass flow rate of the fuel inside the common rail and the manifold insert, for which the following mass balance equation was used.

$$\dot{m}_{fuel(actual)} = \rho_f * A_m * V_e \quad Eq 4$$

Where:

$\dot{m}_{fuel(actual)}$ = Actual mass flow rate of fuel into the intake port (kg.h⁻¹)

ρ_f = Density of the fuel (kg.m⁻³)

A_m = Area of the manifold inserts (m²)

V_e = Exit velocity of the fuel from the manifold insert into the ports (m.s⁻¹)

As the flow of fuel is driven due to pressure difference the exit velocity of the fuel from the manifold inserts was calculated by using the Saint Venant & Wantzel equations, which is an extended form of the Bernoulli's equation for compressible flow [17]. These equations were the basis of the analytical model and will be discussed in the section below. Also, as the injectors are not directly connected to the manifold inserts but have a set of connections in between them to calculate the exit velocities we also had to calculate the velocities & pressure between the intermediate connections. To calculate the velocities & pressures of the intermediate connection between the injector and the manifold inserts following approach was used. If u is the velocity of the fluid at the surface area dS with normal unit vector n then the rate of flow of mass leaving V through that elemental area is as follows.

$$\frac{\partial}{\partial t} \int_V \rho dV = - \oint_S \rho u \cdot n dS \quad Eq 5$$

The above equation is known as the continuity equation in the integral form which states that the rate of change (increase) of mass is equal to the net influx of mass [18] [19]. As the surface area and initial inlet velocities before the injectors were calculated beforehand the equation stated above was used to calculate the intermediate velocities for the connections between the injector and the manifold inserts. To calculate the pressure in the intermediate connection, the velocities obtained from Eq 5 were used along with the energy balance equation.

4.1 Manifold insert fuel exit velocity

As discussed above to calculate the gas exit velocities at the outlet of the manifold inserts it was necessary to know the velocities at the intermediate components. The continuity equation in the integral form looks complicated initially but we can use the conservative form of those equations as follows [18].

$$\rho_1 * A_1 * V_1 = \rho_2 * A_2 * V_2 \quad \text{Eq 6}$$

Where

ρ_1 = Density of the fluid at the inlet (kg.m⁻³)

A_1 = Area of the element at the inlet (m²)

V_1 = Velocity of the fluid element at the inlet (m.s⁻¹)

ρ_2 = Density of the fluid at the outlet (kg.m⁻³)

A_2 = Area of the element at the outlet (m²)

V_2 = Velocity of the fluid element at the outlet (m.s⁻¹)

As the fluid in our case is in the gaseous form the densities at the inlet and outlet of the elements will not be the same due to compression or expansion as it passes through the intermediate component. But as the gas is passing through a series of connections that have a change of diameter ranging between 3 mm to 6 mm the density change would be negligible, hence to simplify the calculation we have considered constant densities. Also, we were able to set the fuel flow from the pressure regulator in the range from 1 bar to 5 bars of absolute pressure, hence we decided to calculate the pressures & velocities of the intermediate components at all possible settings. The dimensions of all the components were known hence the area of all the elements was calculated and was used in Eq 6 along with the values of pressures and velocities of the intermediate component. The area of all the intermediate elements is tabulated below.

Flow-through intermediate connections.		Area [m ²]	Diameter [m]
CR to Injector	a ₁	1.77E-04	1.50E-02
	a ₂	7.07E-06	3.00E-03
Injector to hose	a ₁	7.07E-06	3.00E-03
	a ₂	3.12E-05	6.30E-03
Hose to Tee Split	a ₁	3.12E-05	6.30E-03
	a ₂	1.26E-05	4.00E-03
Tee Split to Hose	a ₁	1.26E-05	4.00E-03
	a ₂	3.12E-05	6.30E-03
Hose to Insert	a ₁	3.12E-05	6.30E-03
	a ₂	9.62E-06	3.50E-03

Table 4.1-1 Area of the elements in intermediate connections.

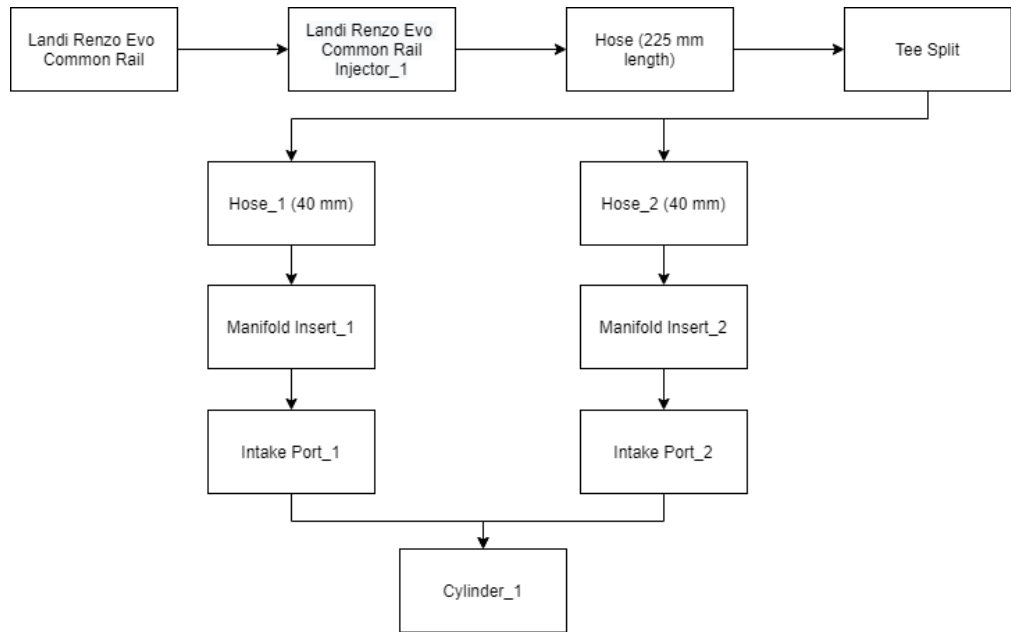


Figure 4.1:1 Schematic of the fuel flow through intermediate components for each cylinder.

Where a_1 is the area of the element at the inlet (CR) and a_2 is the area of the element at the outlet (injector) as so on. The values of velocities at different inlet pressure settings have been tabulated as follows.

Flow-through intermediate connections.		Area [m ²]	I/O	Velocity [m.s ⁻¹] {Using Continuity Equation}				
CR to Injector	a_1	1.77E-04	v_1	14.22	7.02	4.66	3.55	2.832
	a_2	7.07E-06	v_2	355.50	175.50	116.50	88.75	70.800
Injector to hose	a_1	7.07E-06	v_1	355.50	175.50	116.50	88.75	70.800
	a_2	3.12E-05	v_2	80.61	39.80	26.42	20.12	16.054
Hose to Tee Split	a_1	3.12E-05	v_1	80.61	39.80	26.42	20.12	16.054
	a_2	1.26E-05	v_2	199.97	98.72	65.53	49.92	39.825
Tee Split to Hose	a_1	1.26E-05	v_1	199.97	98.72	65.53	49.92	39.825
	a_2	3.12E-05	v_2	80.61	39.80	26.42	20.12	16.054
Hose to Insert	a_1	3.12E-05	v_1	80.61	39.80	26.42	20.12	16.054
	a_2	9.62E-06	v_2	261.18	128.94	85.59	65.20	52.016

Table 4.1-2 Values of velocities for the intermediate connections for different pressure setting from the pressure regulator

Where v_1 is the velocity of the fluid element at the inlet (CR) and v_2 is the velocity of the fluid element at the outlet (injector) as so on. The values of velocities at different inlet pressure settings are shown in Table 4.1-2 which can be used to calculate the pressures of the

intermediate connection using Bernoulli's equation for compressible flow. Figure 4.1:2 (below) shows the variation of the fuel flow velocities as it passed across the intermediate connections at different pressure settings at the pressure regulator. Where P = 1 bar is the output pressure setting of the pressure regulator and so on.

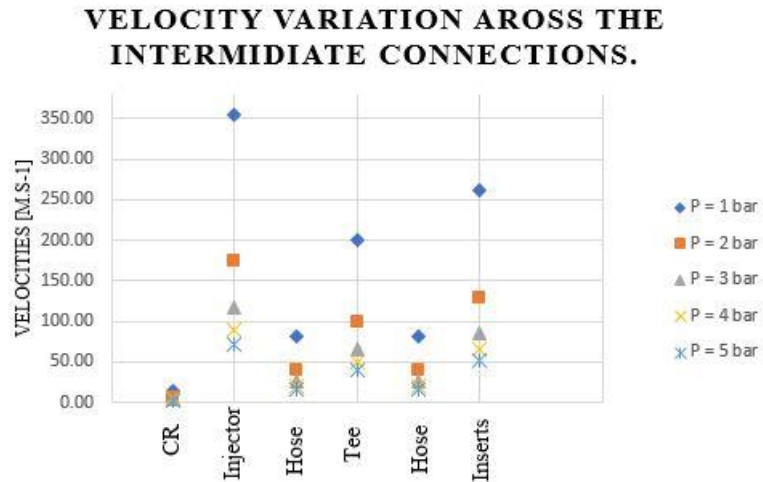


Figure 4.1:2 Flow velocities of fuel across the intermediate connections with different pressure regulator settings.

It can be seen in the above figure that the amplitude of velocity variation across the intermediate connections decreases as the pressure from the pressure regulator increases. Having lower amplitudes of velocities is an advantage as it reduces the chances of flow chocking as the Mach number is less than 1 which means the flow is subsonic [18]. The Bernoulli's equation for compressible flow undergoing adiabatic process from point 1 to 2 is given as follows.

$$\left(\frac{\gamma}{\gamma-1}\right)\frac{p_1}{\rho_1} + \frac{v_1^2}{2g} + z_1 = \left(\frac{\gamma}{\gamma-1}\right)\frac{p_2}{\rho_2} + \frac{v_2^2}{2g} + z_2 \quad Eq 7$$

Where

- γ = Specific heat ratio of fuel
- p_1 = Pressure of fluid element at the inlet (N.m⁻²)
- ρ_1 = Density of the fluid at the inlet (kg.m⁻³)
- v_1 = Velocity of the fluid element at the inlet (m.s⁻¹)
- z_1 = Elevation of the inlet from a reference datum (m)
- p_2 = Pressure of fluid element at the outlet (N.m⁻²)
- ρ_2 = Density of the fluid at the outlet (kg.m⁻³)
- v_2 = Velocity of the fluid element at the outlet (m.s⁻¹)
- z_2 = Elevation of the outlet from a reference datum (m)
- g = Acceleration due to gravity (9.81 m. s⁻²)

The density for methane can be calculated by using the equation of state from thermodynamics which is $pV = mrT$ where p is the pressure of methane in Nm^{-2} , V is the volume occupied in m^3 , m is the mass in kg, r is the specific gas constant in $\text{J.kg}^{-1}.\text{K}^{-1}$ which can be calculated as the ratio of universal gas constant $R = 8.314 \text{ J.mol}^{-1}.\text{K}^{-1}$ to the molecular weight of methane which is 16 g.mol^{-1} , hence the value of $r = 519.62 \text{ J.kg}^{-1}.\text{K}^{-1}$ and T is the temperature of the gas in K. Using the above relation at constant temperature of 293 K, the densities and the heat capacities ratio of methane was tabulated as follows.

Pressure [Nm^{-2}]	1.00E+05	2.00E+05	3.00E+05	4.00E+05	5.00E+05
ρ [kg.m^{-3}]	0.6595	1.38	2.08	2.78	3.482
c_p [$\text{kJ.kg}^{-1} \text{K}^{-1}$]	2.2265	2.2267	2.2329	2.2391	2.2453
c_v [$\text{kJ.kg}^{-1} \text{K}^{-1}$]	1.6970	1.6985	1.6995	1.7006	1.7017
γ	1.31	1.31	1.31	1.32	1.32

Table 4.1-3 Methane density, specific heats & specific heat ratio.

Using the values of densities at the respective pressures and the specific heat ratio from Table 4.1-3 along with Eq 7 the values of the pressures for the intermediate connection were calculated and tabulated as follows.

Flow-through intermediate connections.		Area [m^2]	I/O	Pressure [Nm^{-2}] { Using Bernoulli's Equation }				
CR to Injector	a ₁	1.77E-04	p ₁	1.00E+05	2.00E+05	3.00E+05	4.00E+05	5.00E+05
	a ₂	7.07E-06	p ₂	5.84E+04	1.79E+05	2.86E+05	3.89E+05	4.91E+05
Injector to hose	a ₁	7.07E-06	p ₁	5.84E+04	1.79E+05	2.86E+05	3.89E+05	4.91E+05
	a ₂	3.12E-05	p ₂	9.79E+04	1.99E+05	2.99E+05	3.99E+05	5.00E+05
Hose to Tee Split	a ₁	3.12E-05	p ₁	9.79E+04	1.99E+05	2.99E+05	3.99E+05	5.00E+05
	a ₂	1.26E-05	p ₂	8.69E+04	1.93E+05	2.96E+05	3.97E+05	4.97E+05
Tee Split to Hose	a ₁	1.26E-05	p ₁	8.69E+04	1.93E+05	2.96E+05	3.97E+05	4.97E+05
	a ₂	3.12E-05	p ₂	9.79E+04	1.99E+05	2.99E+05	3.99E+05	5.00E+05
Hose to Insert	a ₁	3.12E-05	p ₁	9.79E+04	1.99E+05	2.99E+05	3.99E+05	5.00E+05
	a ₂	9.62E-06	p ₂	7.76E+04	1.89E+05	2.92E+05	3.94E+05	4.95E+05

Table 4.1-4 Values of pressure for the intermediate connections for different pressure setting from the pressure regulator

Where p_1 is the pressure of the fluid element at the inlet (CR) and p_2 is the pressure of the fluid element at the outlet (injector) as so on. In Figure 4.1:3 (below) we can see pressure

variations across the intermediate connections. Where $P = 1$ bar is the output pressure setting of the pressure regulator and so on. The pressure oscillations in all the settings stabilize as the flow processed and adheres to the values close to the pressure regulator settings.

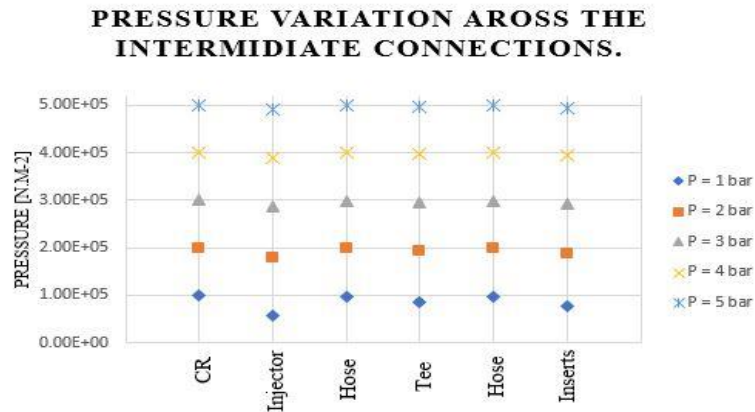


Figure 4.1:3 Pressure of fuel across the intermediate connections with different pressure regulator settings.

As stated earlier the experimental engine is turbocharged and has the pressure after compressor of 2.27 bars and temperature after intercooler as 313 K. But as the flow of air passes from the intake manifold to the intake port there is a pressure drop as there is a change of diameter which is calculated and tabulated as follows.

Intake Manifold Pressure Calculation				
I/O	Diameter [m]	Area [m ²]	Velocities [ms ⁻¹]	Pressure [Nm ⁻²]
Intake Chamber	8.60E-02	5.81E-03	9.12	2.27E+05
Intake Ports	3.85E-02	1.16E-03	45.51	2.25E+05

Table 4.1-5 Intake Manifold & Intake Port pressure calculations

Furthermore, as the intake valve has a lift of 10 mm for CFD simulation purpose there will be an additional pressure drop across the intake valves as well, which is calculated and tabulated as follows.

Flow across the inlet valve							
I/O	Diameter [m]	Lift	Area [m ²]	Velocities [m.s ⁻¹]	Pressure [N.m ⁻²]	Pr. drop across Valve [N.m ⁻²]	Pr. in ports [N.m ⁻²]
Valve Steam	9.00E-03	-	6.36E-05	4.55E+01	2.25E+05	2.88E+04	1.96E+05
Valve Inlet	3.65E-02	1.00E-02	3.01E-04	1.76E+02	1.96E+05		

Table 4.1-6 Pressure drop across the inlet valve and effective pressure inside intake ports

The intake ports will be at a pressure of 1.96 bars which we can round off to 2 bars. Now we have to maintain a constant fuel mass flow rate from the manifold inserts against this intake

port pressure to maintain the required engine output parameters, as we have all the required inputs now we will use the Saint Venant & Wantzel Equation to calculate the fuel exit velocities for the manifold inserts against the intake port pressure of 2 bars. The Saint Venant & Wantzel Equation is as follows [17].

$$v_{\text{exit}} = \sqrt{\frac{2\gamma}{\gamma-1} \frac{p_0}{\rho_0} \left[1 - \left(\frac{p}{p_0} \right)^{\frac{\gamma-1}{\gamma}} \right]} \quad \text{Eq 8}$$

Where

- γ = Specific heat ratio of fuel
- p_0 = Pressure of fluid element upstream (manifold inserts) (N.m⁻²)
- ρ_0 = Density of the fluid at the inlet (kg.m⁻³)
- p = Pressure of fluid element inside the intake port (N.m⁻²)

The exit velocities along and the mass flow of fuel at the respective exit velocities for the pressure regulator setting from 1 to 5 bars were calculated and tabulated as follows.

Pressure Regulator Set. [Nm ⁻²]	3.00E+05	4.00E+05	5.00E+05
Exit Velocities [m.s ⁻¹]	327.86	428.46	486.75
Mass flow rate			
$\dot{m}_{\text{fuel(per insert)}}$ [kg.h ⁻¹]	23.63	41.15	58.70
$\dot{m}_{\text{fuel(per cylinder)}}$ [kg.h ⁻¹]	47.26	82.50	117.39

Table 4.1-7 Exit Velocities & Mass flow rate of fuel according to Saint Venant & Wantzel equation

It can be seen from Table 4.1-7 that there is no mass flow of fuel if the pressure regulator is set at a working pressure of 1 and 2 bars. This is because the pressure inside the intake ports is higher than the pressure inside the fuel manifold inserts, hence under these conditions no flow of fuel is possible. This means that the pressure regulator should be set in such a way that the working pressure should be higher than the intake port pressure. Now to maintain the required engine operating conditions we have calculated the mass flow rate of fuel (see section 3.2) as 18 kg.h⁻¹ which means 4.5 kg.h⁻¹ per cylinder. But it should be noted that the intake valves are not open all the time during the engine operation, also the fuel is not injected for all the time during operation. The intake valves open for few milliseconds and so does the fuel injection event, at a given engine speed during the intake stroke. As we have few milliseconds for which the intake valves are open and fuel is being injected, we can increase the fuel injection time & the mass flow rate to prepare the mixture before the intake stroke begins so we get sufficient time to induct the required amount of air-fuel mixture for the desired engine operating points.

4.2 Mass flow rate sensitivity analysis for one engine cycle.

The experimental engine will be operated at 2200 RPM and for simplification of understanding, we will consider only one cylinder with one engine cycle which needs 4.5 kg.h^{-1} fuel flow rate. If the fuel injection is started when the intake valve is opened exactly when the piston is at TDC and if the fuel injection is stopped when the intake valve is closed exactly when the piston is at BDC, then the time for from the start of injection to end of injection will be done is 13.6 milliseconds i.e. 180-degree rotation of the crankshaft @ 2200 RPM. Which means we have 13.6 milliseconds to deliver the required amount of fuel inside the cylinder. As the time available is reduced the mass flow rate should be increased to compensate for the reduced time and still maintain the instantaneous required fuel mass flow rate required for the desired operation. So, at 13.6 milliseconds available for induction of the fuel inside the cylinder the actual fuel flow rate calculated is 330 kg.h^{-1} per cylinder, this means that if we maintain 330 kg.h^{-1} fuel flow rate only then we will be able to inject 4.5 kg.h^{-1} inside the cylinder to maintain 100 kW power output @ 2200 RPM in 13.6 milliseconds. To see the sensitivity of the above-mentioned phenomena we decided to increment the fuel injection time by 5 degrees BDC & TDC respectively.

Mass flow rate sensitivity calculations.			
SOI (Before TDC)	EOI (After BDC)	Injection time available [milliseconds]	Actual flow rate required per cylinder [kg.h^{-1}]
0	0	13.6	330
5	5	14.4	312
10	10	15.2	297
15	15	15.9	282
20	20	16.7	270
25	25	17.4	258
30	30	18.2	247

Table 4.2-1 Dependency of injection time available on fuel mass flow rate

However, it is possible to inject fuel in the intake ports for one complete cycle which gives us 54.5 milliseconds at given RPM. So, the fuel flow rate required is reduced to 82.50 kg.h^{-1} per cylinder and as each cylinder is equipped with two manifold inserts the fuel flow at each insert is 41.25 kg.h^{-1} . This analysis was done to decide the actual pressure regulator setting to maintain the engine power at 100 kW @ 2200 RPM. Figure 4.2:1 (below) shows the variation of the fuel injection rate v/s time. It can be seen that as the time available for fuel injection increases, the actual fuel flow rate decreases.

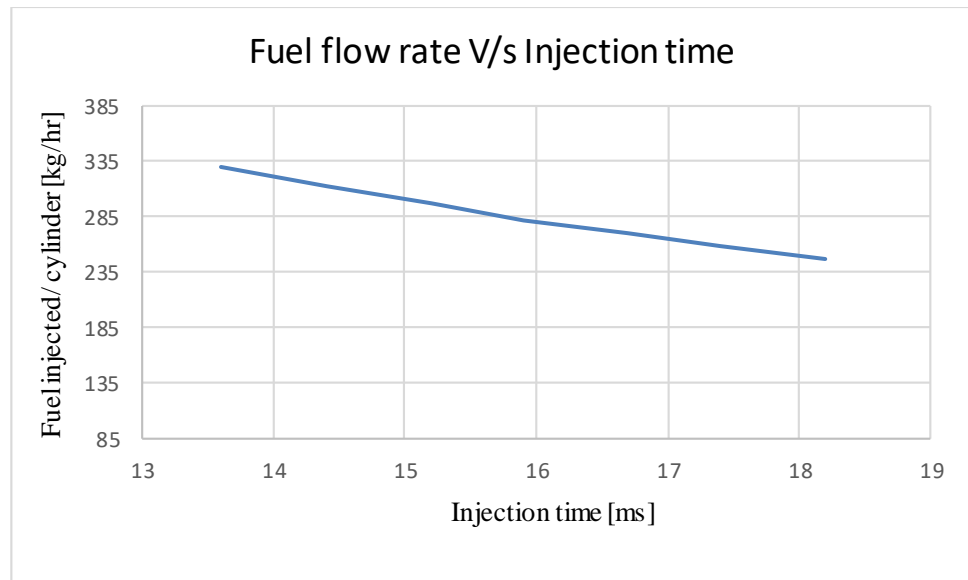


Figure 4.2:1 Dependency of injection time available on fuel mass flow rate

Now if we compare the required value of the fuel flow which is 41.25 kg.h^{-1} per manifold insert from the above-mentioned calculation and with Table 4.1-7 Exit Velocities & Mass flow rate of fuel according to Saint Venant & Wantzel equation & Eq 8 (above), we can see that the current pressure regulator setting of 4 bars pressure gives us 41.15 kg.h^{-1} per manifold insert which is close enough to our required value. Hence if we recalculate the pressure regulator setting to get exactly 41.25 kg.h^{-1} per manifold insert then the pressure regulator needs to be set to a pressure of 4.01 bars for which the pressure before the manifold insert is 4 bars, the exit velocity of fuel at this setting is 428.5 ms^{-1} . The velocity of sound for methane at 4 bars pressure and 293 K is calculated as 449.7 ms^{-1} , hence the Mach number is 0.9 which is less than 1 so the flow inside the manifold inserts is subsonic [18] [19].

5 Part Design

The 3-D CAD model and drawings were created in PTC Creo software. This section refers to the drawing documentation in the attachment outside the thesis. In the beginning, there were several parameters in which the project had to conform. The main constraint was that the engine was lent to us by Zetor which means that all the parts designed must fit a given size with minimum changes to the existing engine design. The design module contains a common rail, injector, hoses to connect the injector to the tee & manifold inserts. The common rail has to be mounted in the central position. All the above-mentioned module parts will be discussed in this section.

The Zetor Z1605 engine is a 4-cylinder 4 stroke compression ignition engine which will be rebuilt as a spark ignited gas engine. The first and most important change for this conversion was mixture preparation. In a compression ignition engine, only air is inducted into the cylinder which is then compressed to higher pressure and the temperature during the compression stroke. Just before the piston reaches TDC diesel fuel at high pressure (up to 2000 bars) is injected into the high pressure & temperature compressed air which initiates the combustion process. Each cylinder is equipped with two intake ports amongst which one port is tangential & the other port is helical which will create high turbulence by introducing in-cylinder swirl which further will ensure rapid mixing of the diesel fuel and air and a diffusion flame will start combustion [8]. But in a spark-ignition engine air-fuel mixture enters the cylinder, which is then compressed and ignited by a spark plug and a stable flame kernel is established which further progresses combustion [8]. In our case to achieve a homogeneous mixture of air and CNG fuel inside the cylinder it was decided to use the already existing port geometry to our advantage by injecting fuel in each intake port. But the Landi Renzo Evo CR consists of only four injectors and the engine had two intake ports per cylinder hence in total we had eight intake ports. To divide the flow from one injector into two individual streams a tee split was used. This arrangement ensured all eight intake ports have fuel supply. Such a fuel injection strategy is known as a multipoint fuel injection system (MPFI).

The common rail was mounted as close as possible to the intake manifold so that the fuel supply hoses have a minimum length. The injector outlet was connected to the tee split inlet with a rubber hose and then tee split outlets were connected to the manifold inserts by the same rubber hose. This connection enabled the least resistance fuel flow path and to ensure proper sealing to avoid gas leak hose clamps were used at each end of the connection of the hose.

5.1 Intake manifold details.

As discussed in section 5 (above) it was decided to inject gas in all the intake ports to achieve a good mixture of air and fuel, the following changes were made to the original engine's intake manifold. Figure 5.1:1 (below) shows the intake manifold which is made of ductile cast iron has eight holes each 5.5 mm in diameter was drilled in each intake port which will house the manifold inserts via threaded joints. The manifold inserts were provided in the Landi Renzo CNG kit which is made of brass and is equipped with standard M6 threads. The holes drilled in the manifold will be threaded by using a standard M6 tapping tool. Refer to ATTACHMENT A drawing number PRO-001-2020 for details.

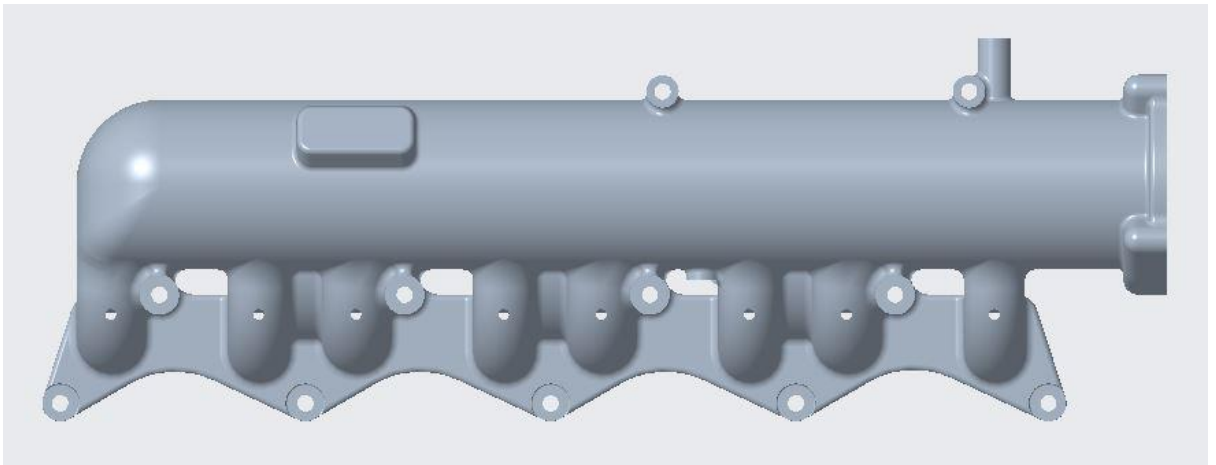


Figure 5.1:1 Top view of the intake manifold with manifold insert holes drilled

Figure 5.1:2 (below) shows the cross-sectional view of the intake manifold where we can see the locations of the holes. The holes were designed in such a way that the direction of flow for the gaseous fuel will be perpendicular to the flow of air which will offer less resistance path to the flow of fuel and will aid proper mixing.

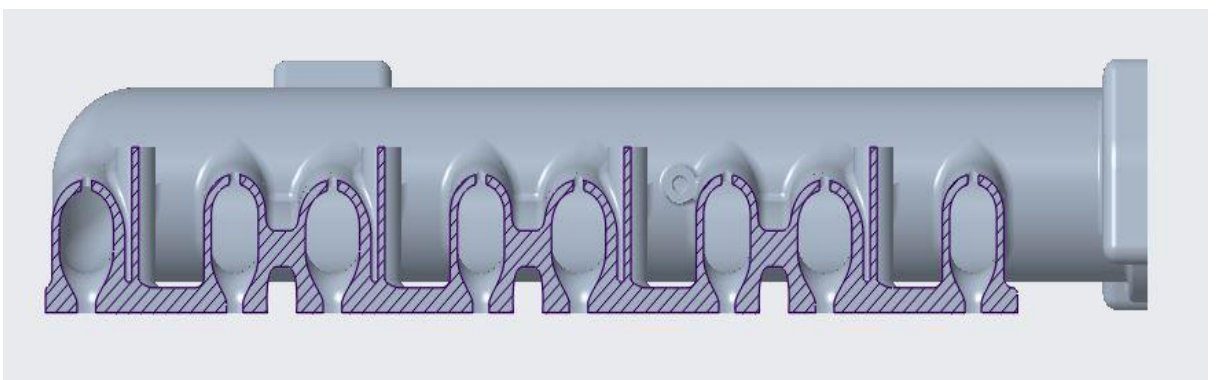


Figure 5.1:2 Front sectional view of the intake manifold with manifold insert holes drilled

Figure 5.1:3 (a) (below) shows the cross-sectional view of the manifold insert which is made of brass. The manifold insert has an inner diameter of 3.5 mm and a total length of 32 mm.

The threading length is 10 mm. The hexagonal-shaped nut above the threading as shown in Figure 5.1:3 (b) (below) can be used to fasten the manifold inserts with the threadings of the intake port holes.

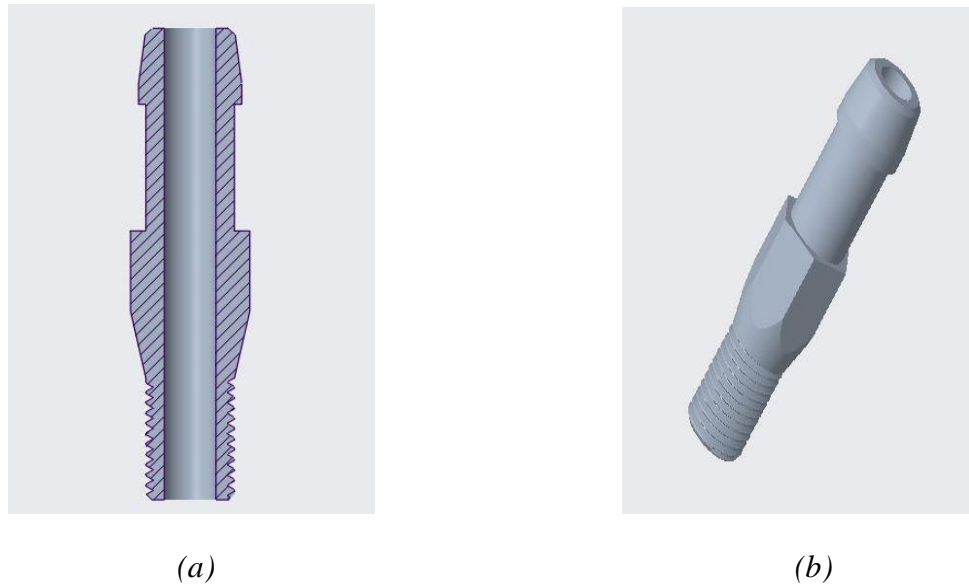


Figure 5.1:3 The manifold inserts which will supply fuel inside the intake ports: (a) Cross-sectional view; (b) 3-D View.

Figure 5.1:4 (below) shows the assembly of the manifold inserts & the intake port holes. The manifold inserts must be tightened only up to a length of 4 mm, further tightening will cause the manifold insert tips to protrude out into the intake port and cause interference with the airflow path. Before tightening the manifold inserts into the intake port holes the threads on the manifold inserts must be wrapped with Teflon tapping and then be assembled. This will ensure that there is no gas leakage through the gaps between the threaded joints. Refer to ATTACHMENT C-3 drawing number DET-003-2020 (sheet no 3 of 4) for details.

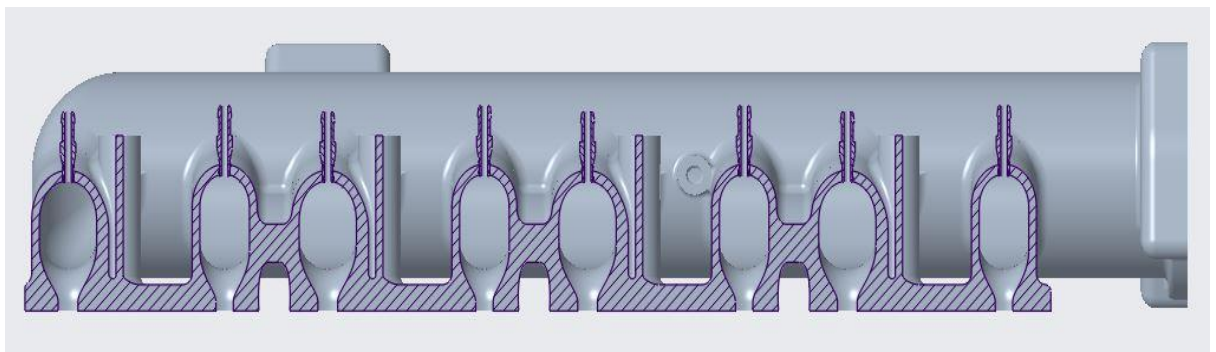


Figure 5.1:4 Front sectional view of the intake manifold with manifold insert assembly

5.2 Holder details

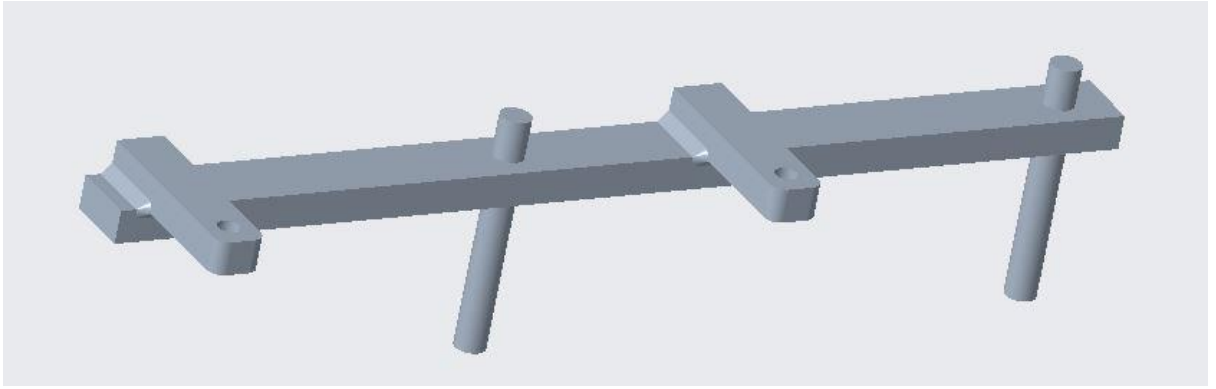


Figure 5.2:1 Common rail holder with stud bolt assembly

Figure 5.2:1 (above) shows the holder assembled with the stud bolts. The material used for manufacturing the holder is S 275 JR (EN 10025). The raw material dimensions 440*20*10 mm. The material will be first cut to the required size and shape are from the raw material. The two holder arms will be first cut to the required size and shape. After that, the holder arms will be drilled, each with one hole of 6 mm diameter. Then the holder arms will be welded to the base plate. The base plate will be drilled with two holes each of 8 mm diameter where the stud bolts will be inserted. The stud bolts will provide the necessary elevation required to keep the holder at a sufficient close height from the manifold as shown in Figure 5.3:1 (below). Refer to ATTACHMENT B drawing number PRO-003-2020 for details.

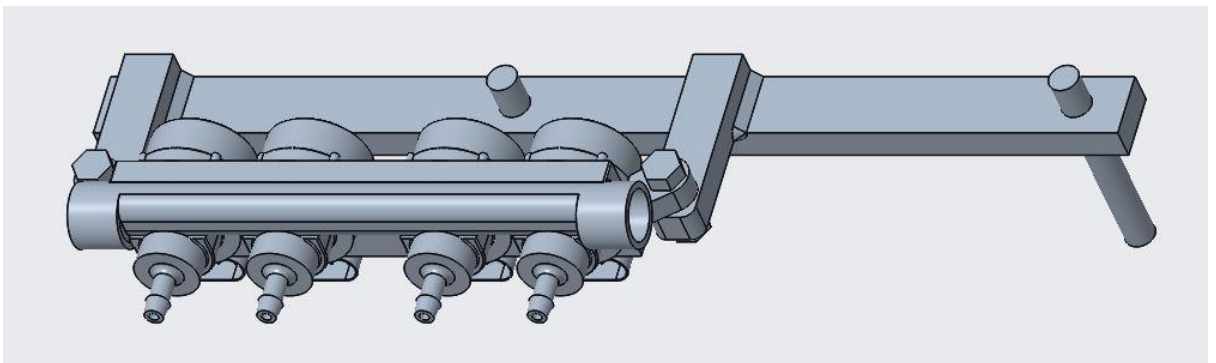


Figure 5.2:2 Common rail with integrated injectors and holder assembly

Figure 5.2:2 (above) shows the assembly of the Landi Renzo common rail with the holder. The common rail will be fixed to the holder using M6 nuts and bolts. The nuts and bolts mounting with the common rail & holder can be seen in Figure 5.2:2 (above), Figure 5.2:3 (below), and Figure 5.2:4 (below).

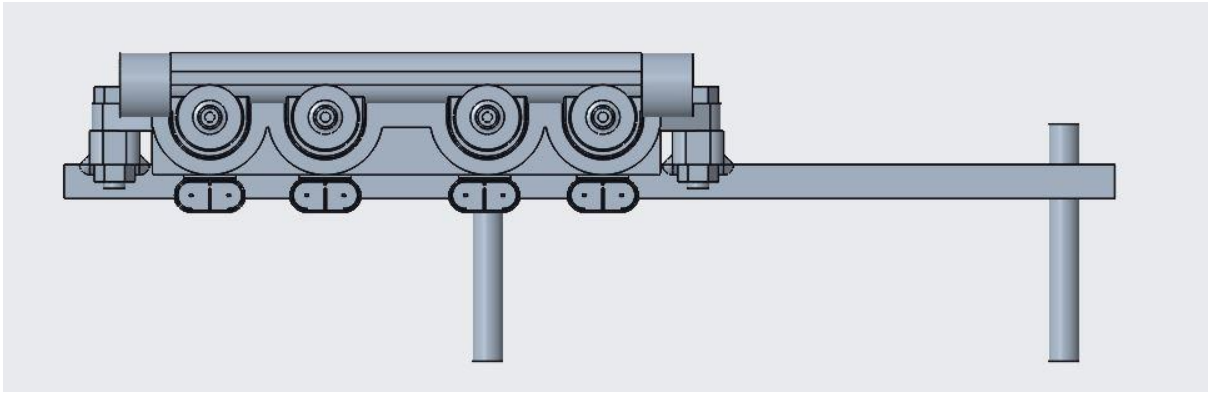


Figure 5.2:3 Front view of common rail with integrated injectors and holder assembly

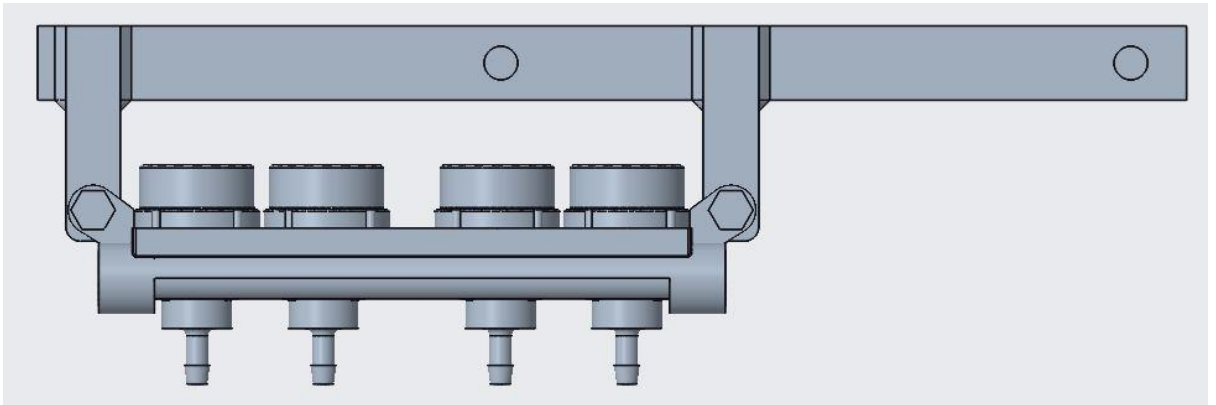


Figure 5.2:4 Top view common rail with integrated injectors and holder assembly

The intake manifold has a predefined fixture which will be used to insert the stud bolts to secure the entire holder and common rail assembly above the manifold which can be seen in Figure 5.3:1 (below). The common rail is made from plastic hence is extremely light weight yet robust. During the engine testing & normal operation, the holder will be subjected to vibrations. But the holder is designed to withstand the weight of the common rails as well as there will be no damage to the holder due to vibrational forces. (Factor of Safety was calculated to be around 8.4 for the holder, hence we can say that the designed holder is over safe.)

5.3 Assembly details

In this section, we shall see the step by step assembly of the entire module with the manifold in details. The intake manifold will be attached to the main engine block by bolts which will be inserted from the holes on both flanges of the manifold into the engine block. After that, the stud bolts of size 8 mm should be inserted into the manifold holes on the top right corner which can be seen in Figure 5.3:1 (below). A distance of 22.5 mm must be maintained between the holder and the manifold. For this purpose, a circular pipe of 15 mm outer diameter and 8 mm inner diameter must be cut to a length of 22.5 mm which will act as a spacer to maintain the required distance. An alternative to the spacer can be done by placing a

combination of washers & M8 nuts on one another to achieve a length of 22.5 mm. After this step, the holder holes should be placed on the stud bolts. To secure the holder and the stud bolts washers should be placed on the top side and the M8 nuts must be used for fastening purposes. Then the manifold inserts must be fastened to the intake manifold. The assembly after the above-mentioned steps is shown in Figure 5.3:1 (below). Refer to ATTACHMENT C-2 drawing number DET-002-2020 (sheet no 2 of 4) for details.

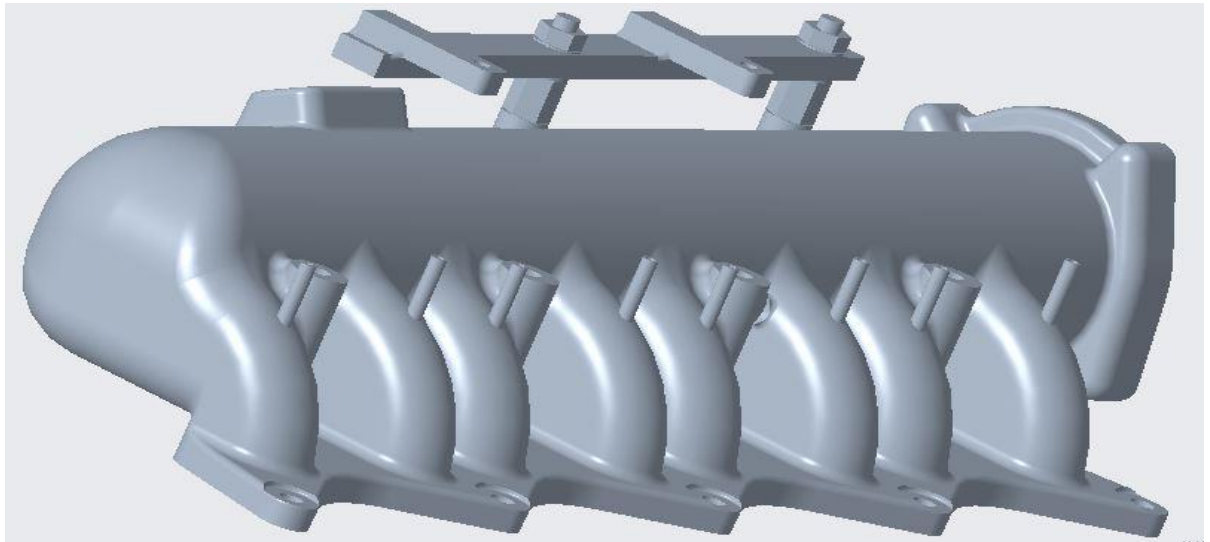


Figure 5.3:1 Intake Manifold, Manifold Inserts & Holder Assembly

The next step is to place the common rail on the holder. The axis of the holes on the holder arms and the axis of holes on the common rail must be matched and then the common rail should be secured on the holder by inserting M6 bolts through the matched holes. Then M6 nuts should be used for fastening purposes. The assembly until now is shown in Figure 5.3:2 (below).

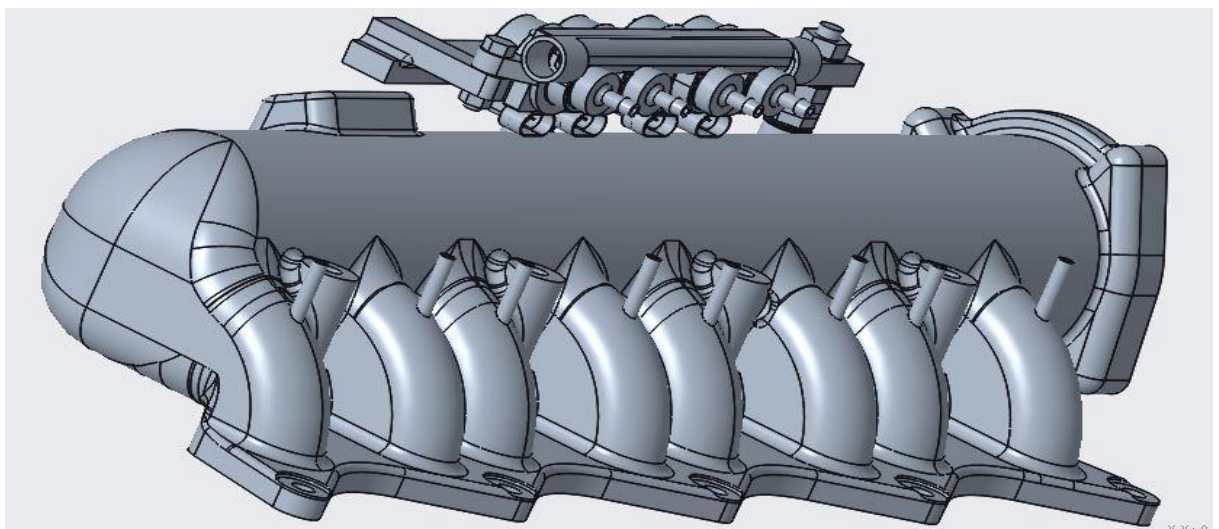


Figure 5.3:2 Intake Manifold, Manifold Inserts, Holder & Common Rail with integrated Injectors Assembly

After the common rail is mounted on the holder, one end of the flexible gas hose of length 225 mm should be connected to the injector tip and a hose clamp should be used to secure the flexible gas hose and injector tip for all four cylinders. The other end of the flexible should be connected to the tee split inlet and again hose clamps must be used to secure the flexible gas hose and tee split inlet. Figure 5.3:3 (below) shows the hoses connecting the injector tips and the tee splits of different length only for aesthetical drawings purpose, it should be noted that all the hoses connecting the injector tips & the tee split in actual use will be equal in length (225 mm length). Please refer to ATTACHMENT C-2 drawing number DET-002-2020 (sheet no 2 of 4) for details. After this one end of the flexible gas hose of length 40 mm should be connected to the outlet of the tee split and a hose clamp should be used to secure the flexible gas hose and outlet of the tee split. The other end of the flexible should be connected to the manifold insert's inlet and again hose clamps must be used to secure the flexible gas hose and the manifold insert's inlet. This procedure should be repeated for connecting the remaining injectors to the manifold inserts. Refer to ATTACHMENT C-2 drawing number DET-002-2020 (sheet no 2 of 4) for details. The complete assembly is shown in Figure 5.3:3 (below).

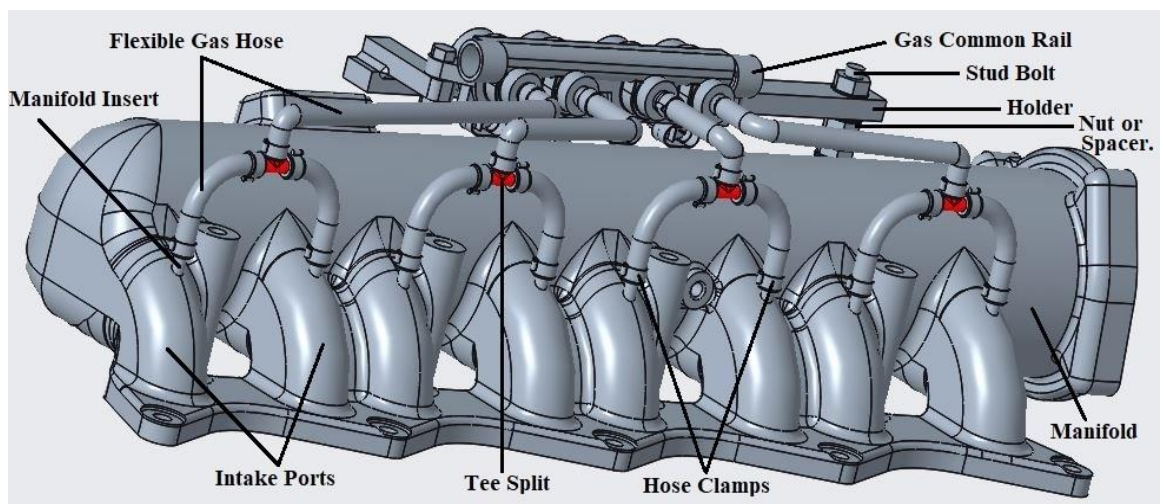


Figure 5.3:3 Complete Module Assembly

5.4 Purchased parts

Considering the cost point of view, it is very important to use mass-produced parts where ever possible. The parts purchased from local suppliers include flexible gas hose, hose clamps, tee split, Landi Renzo Evo CNG kit, washers, nuts, and bolts. The Landi Renzo Evo CNG kit has been shown in Figure 3.2:1 (above) and Figure 3.2:2(above).

5.4.1 Flexible gas hose



Figure 5.4:1 GWPB Flexible Gas Hose

The GWPB flexible hose is suitable for the transport of natural gas and liquefied petroleum products. The hose has an outer diameter of 13.3 mm and an inner diameter of 6.3mm. The working pressure of the hose is up to 20 bars and the working temperature ranges from -30°C to 70°C. Flexible hoses are simple in construction and are easy to mount on different parts of our application.

5.4.2 Hose clamps



Figure 5.4:2 Hose Clamps

The hose clamps have the clamping range of 12-22 mm outer diameters and have a width of 9 mm. They are made of galvanized steel and are suitable for high mechanical loads. The most important feature of the clamp is its structure, which ensures great clamping power and strength. The buckle fits perfectly on the hose and ensures the optimum tightness of the joint.

5.4.3 Tee split



Figure 5.4:3 Tee Split

The tee split is made of polyvinyl acetate resin which has high strength, rigidity, and good chemical reaction resistance. The working pressure is up to 10 bars and the working temperature range is up to 80°C.

Sr No.	Part Name	Drawing No.	Quantity	Supplier	Product Name.
1	Flexible Hose	DET-001-2020	5 meters	Gumex	GWPB Natural Gas & LPG Hose
2	Hose Clamps	DET-001-2020	24	Gumex	Hose clamp TORRO W1
3	Tee Split	DET-001-2020	4	Gumex	TRS - NORMAPLAST COUPLING
4	Bolt M6*25	DET-001-2020	2	Valenta	Hex screws with full thread - zinc-plated DIN 933 - 8.8
5	Nut M6*5	DET-001-2020	2	Valenta	Hex nut - DIN 934, ČSN 02 1401
6	Stud M8 Bolt	DET-001-2020	2	Valenta	Dowel screws - total-thread
7	Nut M8*6.5	DET-001-2020	8	Valenta	Hex nut - DIN 934, ČSN 02 1401
8	Washer M8*1.6	DET-001-2020	12	Valenta	Flat washers - DIN 125 A, ČSN 02 1702

Table 5.4-1 List of purchased material & suppliers

Up till now, we have discussed the design changes made to the engine along with the technical drawings & assembly and component selection for the conversion CI engine to spark-ignited CNG engine. We have also described the port fuel injection control strategy for methane fuel which completes the primary objective of this thesis. Now we shall discuss the secondary objective of the thesis that is 3-D CFD & simulations using the engine configurations discussed until now.

6 AVL FIRE Simulation

The 3-D CFD simulation is characterized as the most sophisticated approach for the detailed numerical investigations of the fluid motion without loss of information in any domain. The primary reason for using 3-D CFD simulation is to understand flow development and mixing of fuel inside the intake ports & the cylinder and then if required modify the design to achieve desired results. Another extremely important reason to use 3-D CFD is that the modification required to be made to the existing design based on simulations results is much faster and cheaper than the actual production and experimental testing of prototypes.

The AVL FIRE software uses the finite volume discretization method which requires an integral form of the basic conservation laws. The flow of fluid which is in the gaseous or liquid state is governed by the partial differential equations which represent the basic conservation laws for the mass, momentum, and energy balance. The basic conservation laws completely cover the behavior of the fluid system. The CFD software usually solves these partial differential equations by a set of algebraic equations [20]. Now we recall Eq 5 from section 4 which is as follows.

$$\frac{\partial}{\partial t} \int_V \rho dV = - \oint_S \rho u \cdot n dS$$

This mass conservation law in its integral form implies that the mass cannot be created from the system, nor it can be destroyed but the mass can be only transferred from one state to another through convection. This equation of mass conservation is additionally called as the continuity equation. The left-hand side of the equation shows the rate of a change of the mass and the right side of the equation shows the net inflow of the mass denoted by a negative sign which means the inflow. Hence the rate of a change of the mass is equal to a net inflow of the mass [20] [21]. Newton's second law of motion describes the conservation of momentum.

$$\frac{d(mv)}{dt} = \sum F \quad \text{Eq 9}$$

Momentum is a vector quantity that is defined as the product of a mass and velocity. The momentum conservation law in the integral form is as follows:

$$\frac{\partial}{\partial t} \int \rho u dV = - \oint \rho u u \cdot n dS - \oint p n dS + \oint 2\mu D \cdot n dS + \int \rho f dv \quad \text{Eq 10}$$

The left-hand side of the equation shows the rate of a change of the momentum and the right-hand side of the equation shows the net inflow of the momentum, total pressure, total viscous

force, and total body force respectively. The surface force term arising due to the pressure and stresses are from the molecular point of view, the microscopic momentum fluxes across that surface [20].

The total energy of the system is the sum of all macroscopic & microscopic energy forms where the macroscopic energy forms constitute the kinetic & potential energy whereas the microscopic energy form constitutes the internal energy of the system [21].

$$\Delta E = \Delta U + \Delta E_k + \Delta E_p \quad \text{Eq 11}$$

The energy conservation law in the integral form is as follows:

$$\frac{\partial}{\partial t} \int \rho \left(e + \frac{1}{2} U^2 \right) dV = - \oint \rho \left(e + \frac{1}{2} U^2 \right) \mathbf{u} \cdot \mathbf{n} dS + \int_V \mathbf{u} \cdot \mathbf{f} dv + \oint \mathbf{n} \cdot (\mathbf{uT}) dS - \oint \mathbf{n} \cdot \mathbf{q} ds$$

Eq 12

The left-hand side of the equation shows the rate of change of the kinetic and internal energy. The right-hand side of the equation shows the net inflow of the kinetic and the internal energy, the work done by body forces, the net work done the stress tensor, and the net heat flow respectively.

Reynolds number is one of the foremost significant dimensionless quantity which is used in the fluid dynamics. It is the ratio of momentum convection and diffusion. Higher Reynold's number means the lower influence of the friction forces of molecules of the fluid on the overall friction. The flow is taken into account as turbulent if Reynold's number exceeds the critical value [18] [20] [21].

$$Re = \frac{uL}{\nu} \quad \text{Eq 13}$$

The turbulent flow is characterized as a three dimensional unsteady and chaotic flow where the fluid particle has random motion in any direction. The increase in turbulence results in an increase of the rate at which the conserved quantities are stirred, the actual mixing is accomplished by a phenomenon called diffusion which is also known as the turbulent diffusion. The well-known Navier-Stokes equations, appended by the empirical law for the dependence of viscosity and thermal conductivity with other flow variables by a constitutive law defining the nature of the fluid, completely describe all the flow phenomena of the Newtonian fluid. If the velocity gradients decrease due to the action of viscosity it also

reduces the kinetic energy of the flow. The energy lost in this process is irreversibly converted into the internal energy of the fluid. When chemical mixing or heat transfer is required then intense mixing is useful. By introducing turbulence both of these properties may be increased by a significant order of magnitude [19] [20].

For turbulent flow simulation, several investigation models such as RANS (Reynolds Averaged Navier-Stokes), LES (Large Eddy Simulation) or DNS (Direct Numerical Solution) are available. The FIRE™ solver uses the RANS (Reynolds Averaged Navier-Stokes) approach. The turbulent quantities are decomposed into the fluctuation part and the average. This decomposition is mentioned in the following equation.

$$a = \bar{A} + A' \quad \text{Eq 14}$$

Where \bar{A} is a time-averaged turbulent quantity and T is the time which has to be large enough compared to the time scale of the turbulence but still small enough as compared to the time scales of all other unsteady phenomena. The A' is the turbulent fluctuating part which is of the stochastic. Now for the pressure and velocity decomposition, we can use Eq 14 as follows.

$$p = \bar{p} + p' \quad \text{Eq 15}$$

$$u = \bar{u} + u' \quad \text{Eq 16}$$

For the steady-state turbulent flow, we can use time-averaging which can be done as follows.

$$a'' = \frac{1}{T} \int_0^T a \, dt \quad \text{Eq 17}$$

Whereas for the homogeneous turbulent flow, we can use space averaging which can be done as follows.

$$a'' = \frac{1}{L} \int_0^L a \, dx \quad \text{Eq 18}$$

Eq 17 and Eq 18 of the turbulence energy model were introduced to understand the governing equations and models which the software uses. However, in our case, the $k - \epsilon$ model is used. This model is based on the specific kinetic energy that means it is the kinetic energy per unit mass basis. This specific kinetic energy model is stated as follows.

$$k = \frac{1}{2} (\overline{u'^2} + \overline{v'^2} + \overline{w'^2}) \quad Eq 19$$

Where u , v , and w are velocity vectors in x , y , and z -direction respectively. Now to proceed further we need to introduce Reynold's stress tensor as the specific kinetic energy is proportional to Reynold's stress tensor.

$$\tau_{ij} = 2\mu_T S_{ij} - \frac{2}{3} \rho k \delta_{ij} \quad Eq 20$$

For the compressible flow model after the substitution, the turbulence kinetic energy equations are derived. This is suitable for all the energy equation models also, the model can be used for the computation of the specific kinetic energy k as well as for the turbulent length scale l [22].

$$\rho \frac{\partial k}{\partial t} + \rho U_j \frac{\partial k}{\partial x_j} = \tau_{ij} \frac{\partial U_i}{\partial x_j} - \rho \epsilon + \frac{\partial}{\partial x_j} \left[\left(\mu + \frac{\mu_T}{\sigma_k} \right) \frac{\partial k}{\partial x_j} \right] \quad Eq 21$$

Eq 20 which is the equation for Reynolds stress tensor and Eq 21 for the turbulence kinetic energy is based on the Boussinesq approximation. The main theory is to derive the exact equation for the dissipation per unit mass ϵ and find all other equations governing its behavior. Navier-Stokes can be used to derive ϵ [22] [23].

$$\begin{aligned} \rho \frac{\partial \epsilon}{\partial t} + \rho U_j \frac{\partial \epsilon}{\partial x_j} = & 2\mu [\overline{u'_{i,k} u'_{j,k}} + \overline{u'_{k,i} u'_{k,j}}] \frac{\partial U_i}{\partial x_j} - 2\mu \overline{u'_k u'_{i,j}} \frac{\partial^2 U_i}{\partial x_k \partial x_j} - 2\mu \overline{u'_{i,k} u'_{i,m} u'_{k,m}} \\ & - 2\mu \overline{u'_{i,k} u'_{i,m} u'_{k,m}} - 2\mu \nu \overline{u'_{i,k m} u'_{i,km}} + \frac{\partial}{\partial x_j} \left[\mu \frac{\partial \epsilon}{\partial x_j} - \overline{\mu u'_j u'_{i,m} u'_{i,m}} - 2\nu \overline{p'_m u'_{j,m}} \right] \end{aligned} \quad Eq 22$$

Where the right-hand side of the equation the first and the second component are the production of dissipation, the third and the fourth component states the dissipation and the last component is the sum of the molecular diffusion of dissipation and the turbulent transport of dissipation. This equation is extremely complicated than the turbulence kinetic energy equation and consists of several new unknown double and triple correlations of fluctuating velocity, pressure, and velocity gradients. The standard $k - \epsilon$ model is as follows [22].

Kinematic Eddy Viscosity:

$$\mu_T = \rho C_\mu \frac{k^2}{\epsilon} \quad Eq 23$$

Turbulence kinetic energy:

$$\rho \frac{\partial k}{\partial t} + \rho U_j \frac{\partial k}{\partial x_j} = \tau_{ij} \frac{\partial U_i}{\partial x_j} - \rho \epsilon + \frac{\partial}{\partial x_j} \left[\left(\mu + \frac{\mu_T}{\sigma_k} \right) \frac{\partial k}{\partial x_j} \right] \quad Eq 24$$

Dissipation rate:

$$\rho \frac{\partial \epsilon}{\partial t} + \rho U_j \frac{\partial \epsilon}{\partial x_j} = C_{\epsilon 1} \frac{\epsilon}{k} \tau_{ij} \frac{\partial U_i}{\partial x_j} - C_{\epsilon 2} \rho \frac{\epsilon^2}{k} + \frac{\partial}{\partial x_j} \left[\left(\mu + \frac{\mu_T}{\sigma_k} \right) \frac{\partial \epsilon}{\partial x_j} \right] \quad Eq 25$$

Turbulent length scale:

$$l = \frac{C_\mu k^{\frac{3}{2}}}{\epsilon} \quad Eq 26$$

The closure coefficients for the k - ϵ model are $C_{\epsilon 1} = 1.44$, $C_{\epsilon 2} = 1.92$, $C_\mu = 0.09$, $\sigma_k = 1.0$, and $\sigma_\epsilon = 1.3$ [22].

The 3-D CFD modeling and investigations are an approximation method hence we have to set a certainly acceptable convergence criterion. If we set higher convergence criteria the simulation will be faster but it will result in less accurate results and vice versa. Also setting up a sufficient number of iteration steps for the convergence is extremely important, from the accuracy points of view. The more iteration steps we set, it consumes more time however, the results are more accurate. Any numerical method is said to be converging if the solution of the discretized equations reaches the exact solution of the differential equation in the model as the grid spacing reaches to zero. The convergence is checked using the convergence monitor from many experiments and past simulation experience. The iterative method converges if

$$\lim_{n \rightarrow +\infty} \epsilon^n = 0 \quad Eq 27$$

Estimating the iteration error to decide when to stop iterating is an important factor in such a numerical investigation. The solver is stopped if the solution starts to diverge from the convergence criteria set by the user. The equations used to solve the model are usually represented by under relaxation factors. Setting up an optimum under relaxation factors purely depends on the problem. An effective strategy is to use a small under relaxation factor in the early iterations and gradually increase them. Having control over the time step is then necessary for controlling the evolution of the solution.

6.1 Simulation Case Setup & Boundary Conditions.

This section deals with the simulation model, step by step setup, the origin of boundary conditions and the initial conditions of the case setup. The aim of the thesis is not to perform a full transient simulation but to set up a case for a steady-state investigation of the air-fuel mixture development. It is important to emphasize that this simulation considers the piston and the intake valves in a predefined stationary position. The intake valves were set to a lift of 10 mm and the length of the cylinder shows the equivalent piston stroke for the specified valve lift, furthermore, the case setup does not simulate the high-pressure phase of the engine cycle. The simulation purely focuses on the development of the air-fuel mixture after the injection of the methane inside the intake ports through the manifold inserts where the flow continues to develop in the engine cylinder as well. All the dimensions and the shape used for the simulations are given by already existing design which has been discussed in section 5. As 3-D CFD simulations are extremely time-consuming as well as computationally demanding, it was decided to simulate the case for one cylinder only. The first step is to create a suitable volumetric geometry file using CAD software, in this case, CREO software was used. Then the CAD geometry is imported into AVL FIRE M where the volumetric geometry was cleaned using surface repair workflow tools for further processing. After this step, the necessary surface, face, and edges selections were made wherein the future we shall define refinement setting in meshing and the boundary conditions. Then the volumetric geometry is meshed using FIRE FAME HEXA™ which is the mesh tool of AVL FIRE™ software. As only air is present at the inlet of intake manifold the max cell size was defined as 3.5 mm as the fine mesh is not required at the inlet section of the intake manifold as there is no mixing of air-fuel. Now to make keep the number of mesh cells in check refined mesh was applied only in the area of particular interest. To do so the feature datum objects were used, which allows us to select a particular area of the geometry and creates an envelope of our required dimension around it. This ensures that only the enclosed area in the selected datum object is refined in the mesh which reduces non-important surfaces from fine meshing. The volumetric mesh is shown in Figure 6.1:1 Volumetric Mesh with grid. The total number of cells was 3.5 million which is typical for such type of simulations.

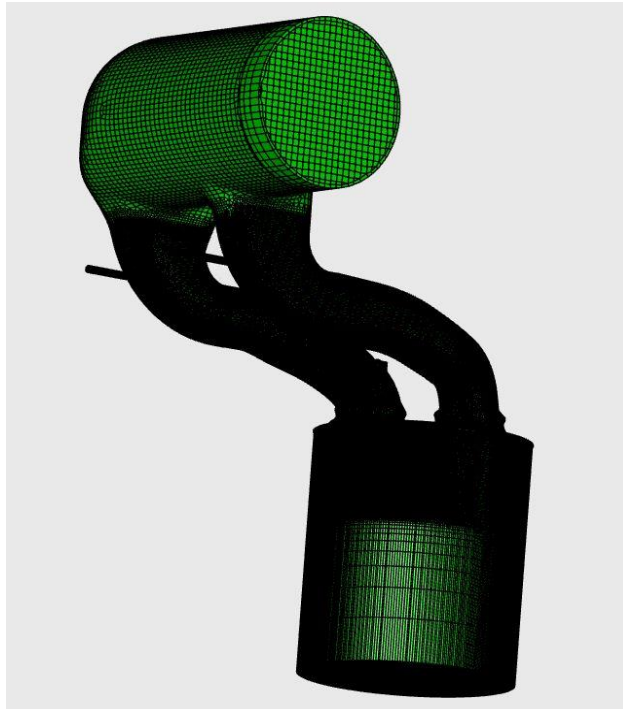


Figure 6.1:1 Volumetric Mesh with grid

The intake ports, methane inlet ports (manifold inserts), and the top section of the cylinder are of primary interest in the flow mixing and development. After creating the datum object for these areas mesh refinement was done using the datum object discretization settings available in the meshing tool. The mesh refinement was set to 3 on the maximum cell size which means each cell of 3.5 mm will be divided into 3 new equal cells each of 1.67 mm. The edge selection named “_REF_EDGE_CYL” was set to have the refinement of 3 up to a depth of 1 mm resulting in a cell size of $4.375e^{-4}$ m, this edge selection was used to map the upper cylinder edge to capture the surface in a circular shape. The edge selection named “_REF_EDGE_1” was set to have the refinement of 7 up to a depth of 1.75 mm resulting in a cell size of $2.734e^{-5}$ m, this edge selection was used to map the methane port inlets to capture the surface in a circular shape. The edge selection was necessary because having fine meshing at the methane inlets was necessary to avoid high inlet velocities (due to coarse mesh if not refined) which would also result in high Mach number where the fuel flow might get choked due to high-pressure waves set up near the inlet from these high-velocity flow. This would also result in simulation errors and have poor convergence. Figure 6.1:2 shows a detailed view of the mesh in an important area of interest.

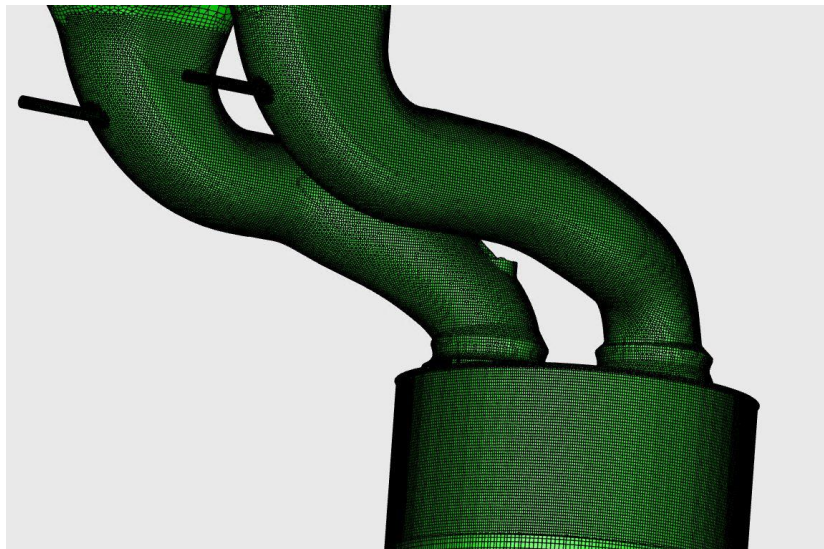


Figure 6.1:2 The intake ports, methane inlet ports (manifold inserts) and the cylinder detailed meshing grid

The mesh file was then imported in FIRE Workflow Manager-FAME Motion for setting the solver steering file (.SSF) which contains all the necessary data of the boundary conditions and initial conditions. The data for boundary conditions and initial conditions are used from section 4.1 and 4.2, some boundary conditions are from the 1-D GT-Power model which is validated by an experimental engine.

The solver steering file is based on the following inputs & assumptions.

Input Parameter	Value / Assumption
Time step	0.001 to 0.2 s
Combustion module	Off
The mixture of air and methane is an ideal compressible gas	Ideal compressible gas
Momentum & Continuity equation	On
Energy equation	On
Turbulence model used	k - ϵ
Species transport module	On
Potential flow initialization mode	On
Fuel mass fraction at the methane inlet port	1
Fuel mass fraction at the air inlet port	0

Table 6.1-1 Solver Steering File inputs & assumptions

Boundary conditions such as the temperature and the pressure of air and methane should be non-negative values. The fuel mass fraction at methane inlet is set as 1 which means only methane flows through both the methane inlet boundary selection.

The boundary conditions on the surface selection are as follows.

Surface Selection Name	Value
BND_Air_Inlet	2.27 (bars of absolute pressure) @ 313 K Temperature
BND_Methane_In_1	4.0 (bars of absolute pressure) @ 293 K Temperature
BND_Methane_In_2	4.0 (bars of absolute pressure) @ 293 K Temperature
BND_Mixture_Out	2.05 (bars of absolute pressure)

Table 6.1-2 SSF Inputs for the boundary conditions on the surface selection.

The under relaxation factor for the momentum is 0.09 in the range of the time step from $50e^{-5}$ s to $200e^{-5}$ s, then 0.099 in the range of the time step from $200e^{-5}$ s to $1000e^{-5}$ s, then 0.2004 in the range of the time step from $1000e^{-5}$ s to $2000e^{-5}$ s and for the rest of the simulation it is 0.2003. Similarly for the pressure it 0.09 in the range of the time step from $50e^{-5}$ s to $100e^{-5}$ s, then 0.1 in the range of the time step from $100e^{-5}$ s to $1000e^{-5}$ s, then 0.2002 in the range of the time step from $1000e^{-5}$ s to $3000e^{-5}$ s, then 0.5002 in the range of the time step from $3000e^{-5}$ s to $5000e^{-5}$ s and then 0.6005 in the range of the time step from $5000e^{-5}$ s to $15000e^{-5}$ s. Turbulent kinetic energy and turbulent dissipation rate have an under-relaxation factor of 0.1 to 0.4 for the same time steps as that are for momentum in the simulation. The energy and species transport equations have an under-relaxation factor of 0.3 to 0.8. The mass source and the viscosity have an under-relaxation factor of 1 and the scalar equations have an under-relaxation factor of 0.8 for the whole simulation. The convergence criteria are set for the pressure, momentum, energy, and scalar equations, all of these equations have the convergence value set to 0.0001 with a maximum number of iterations per each step is 100.

6.2 Simulation Results.

The most significant factor which governs the result is the accuracy of chosen boundary conditions and the initial conditions. However, the accuracy of the result is also given by mesh quality, the damping (under relaxation factor) set for the equations used to solve the case & the convergence criteria. All of the above-mentioned parameters are closely control the computational time as well, hence an optimal setting is need to be applied to get accurate get results in a sufficiently short period. The solver was set for mapping of several different parameters, but as this is the initial stage of the simulation our main interest was to map the mass fraction of methane which would help to investigate the mixing of air-fuel, the flow velocities & Mach number to investigate if the flow was subsonic, sonic or supersonic. Figure 6.2:1 shows the CH_4 mass fraction distribution inside the cylinder. As a reference, the mass fraction of methane which corresponds to lambda 1 was calculated as 0.058 for the air-fuel

mixture. This means that any value higher than the mass fraction 0.058 indicates a rich air-fuel mixture whereas any value lower than the mass fraction 0.058 indicates a lean air-fuel mixture. The mass fraction is seen to vary from 0.0348 to 0.058 from Figure 6.2:1

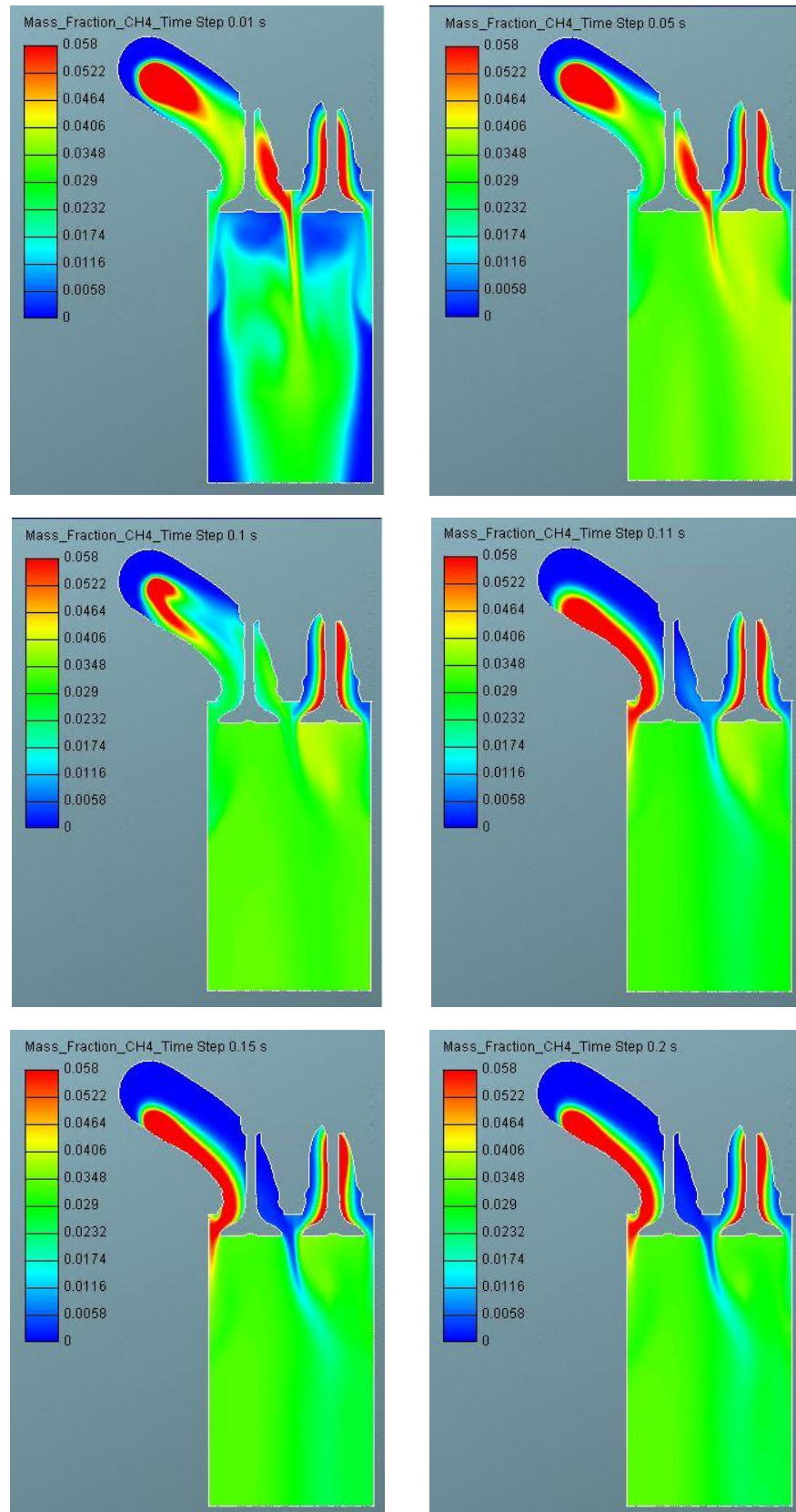


Figure 6.2:1 CH₄ Mass Fraction Mapping for different time steps in seconds.

Mass fraction of CH₄ in one of the intake ports from the side view is shown in Figure 6.2:2

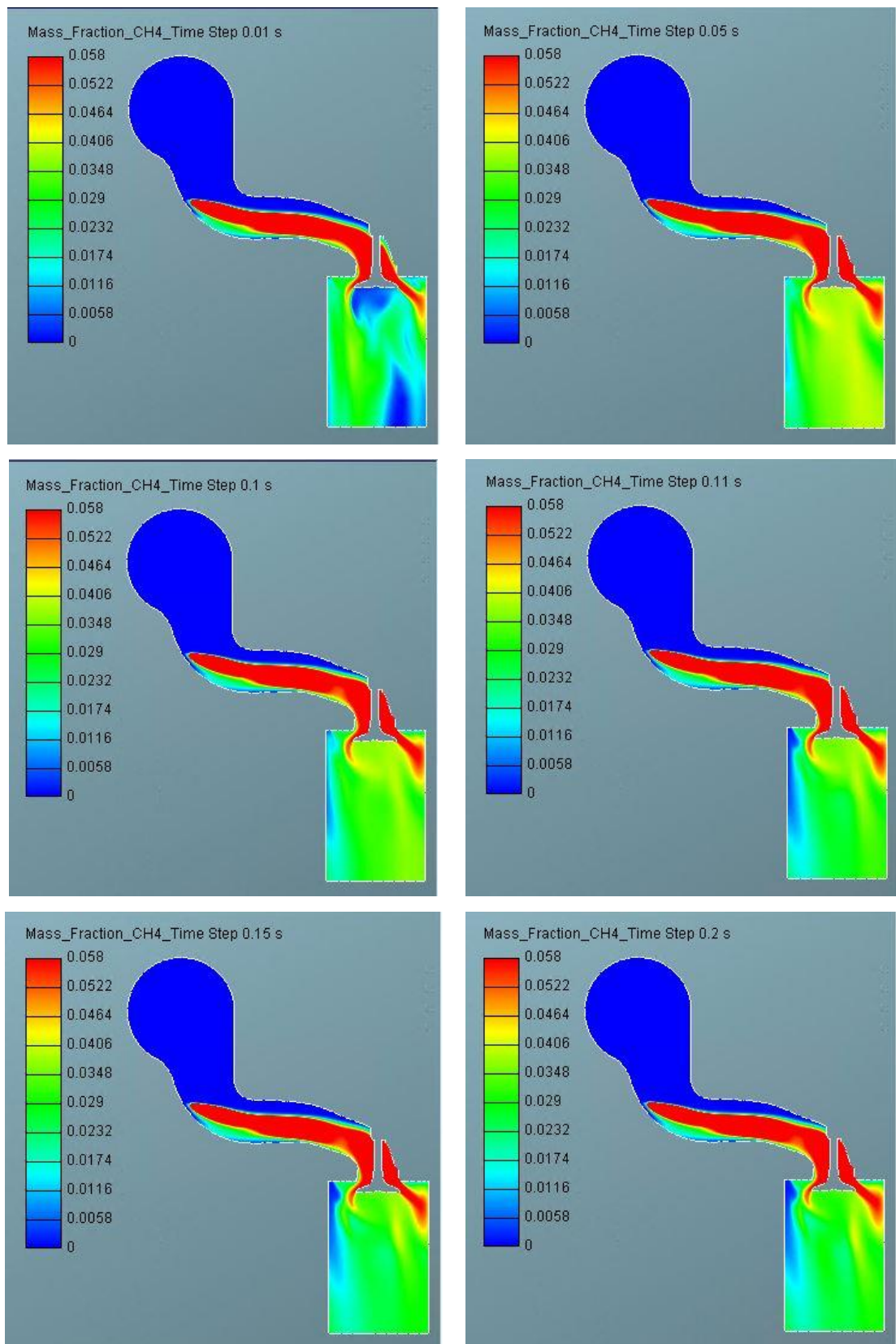


Figure 6.2:2 Mass fraction mapping for one of the intake port from the side view and the start point of methane injection for different time steps in seconds.

Figure 6.2:1 & Figure 6.2:2 we can see that the methane flow profile tries to stick to the intake port's curved surface, this phenomenon is called as the Coanda effect [24] [25].

The mass fraction of CH₄ in the manifold inserts is shown in Figure 6.2:3.

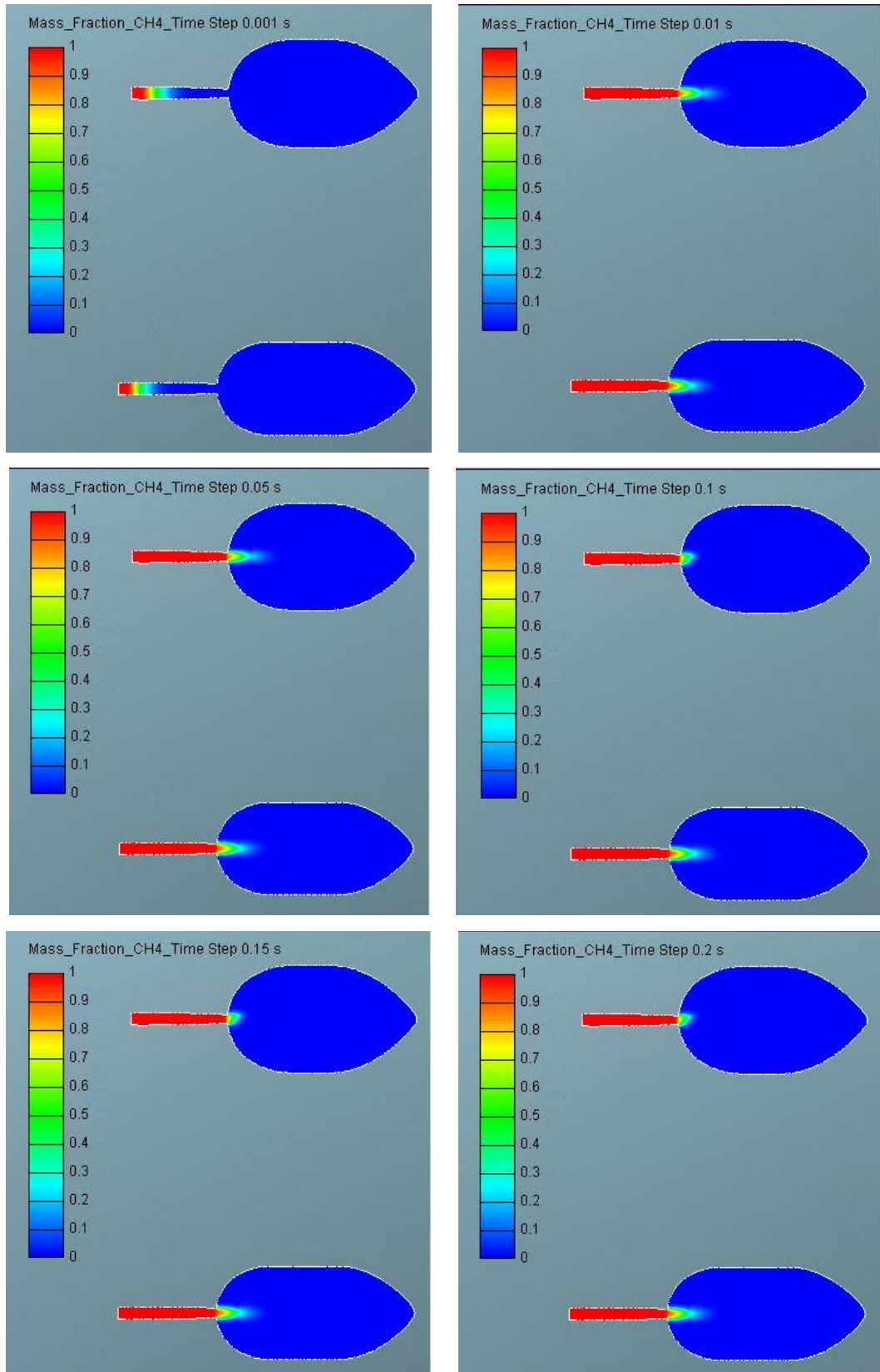


Figure 6.2:3 CH₄ Mass Fraction Mapping for manifold inserts for different time steps in seconds.

We can see that the mass fraction is 1 which means inside the manifold inserts there is only methane fuel present. The fuel jet at the exit of manifold inserts was expected to hit the opposite surface of the intake port due to its inertia as the injection pressure for methane is

higher (4 bars) whereas the air is at a pressure of 2.25 bars inside the intake ports. But due to the combination of intake port pressure and the Coanda effect instead of hitting the opposite surface of the intake port the methane fuel jet seems to have bent in downwards direction towards the intake valves. Also, a diffusive type of air-fuel mixing can be seen in Figure 6.2:2 as the methane jet comes in contact with the compressed air from the turbocharger, where the fuel core remains rich and the adjacent layer of mixture tends to get leaner.

The mass fraction of CH₄ for different layers inside the cylinder is shown in Figure 6.2:4 where all the distances between each layer are referenced to the cylinder head surface.

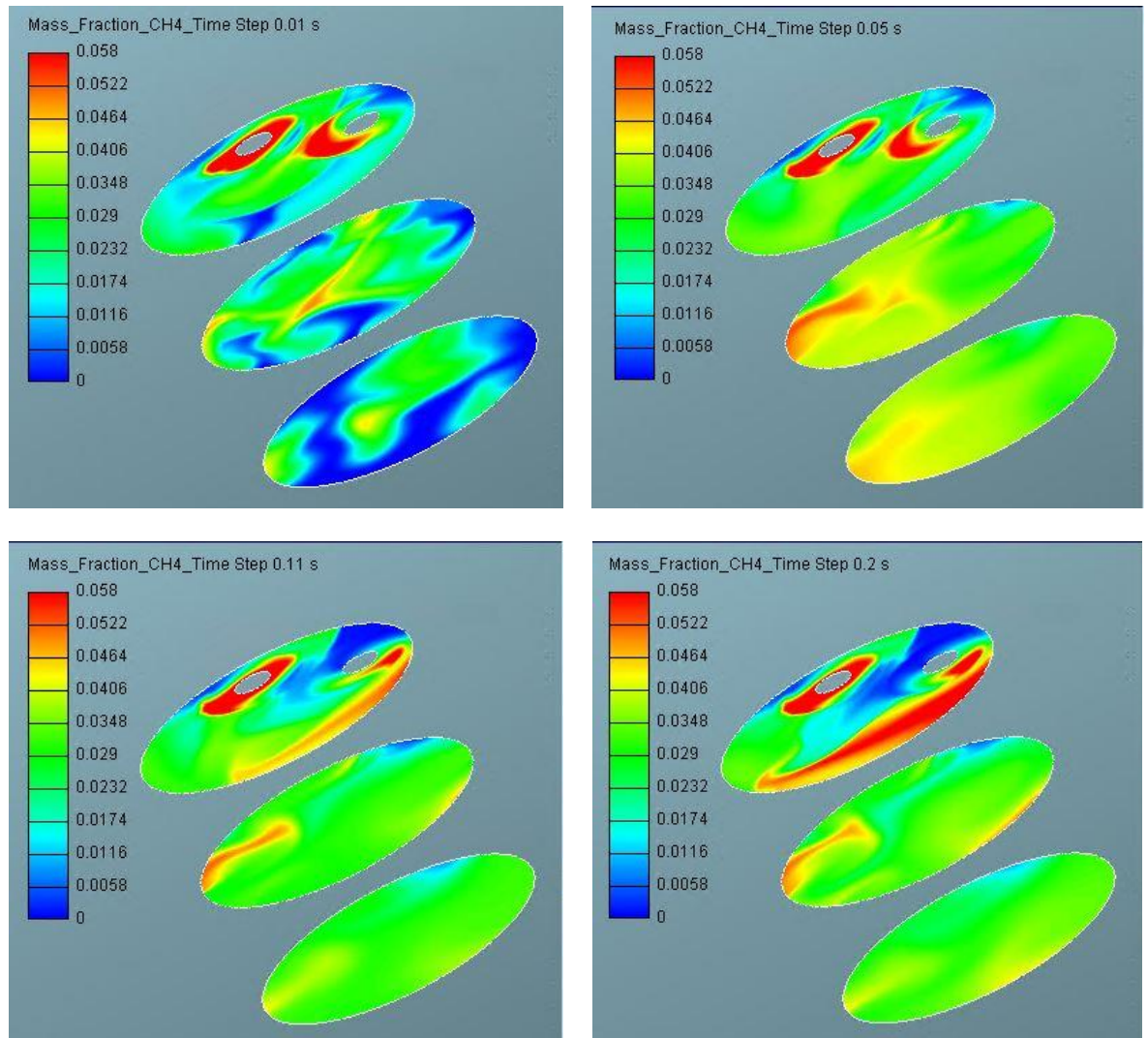


Figure 6.2:4 CH₄ Mass Fraction Mapping for the top layer -10mm, middle layer -50mm and bottom layer -100mm from the cylinder head for different time steps in seconds.

The original experimental engine is a CI engine which will be rebuilt into an SI gas engine, we can see that the mixing is initially stronger near the cylinder head & the valve seats which was expected as this is the mixing strategy used by the CI engines where the diesel fuel is injected in the later phase of the compression stroke. Unfortunately, it is difficult to predict & comment on the average mass fraction & lambda as this is a non-dynamic mesh simulation.

The Mach number of flows inside the cylinder is shown in Figure 6.2:5.

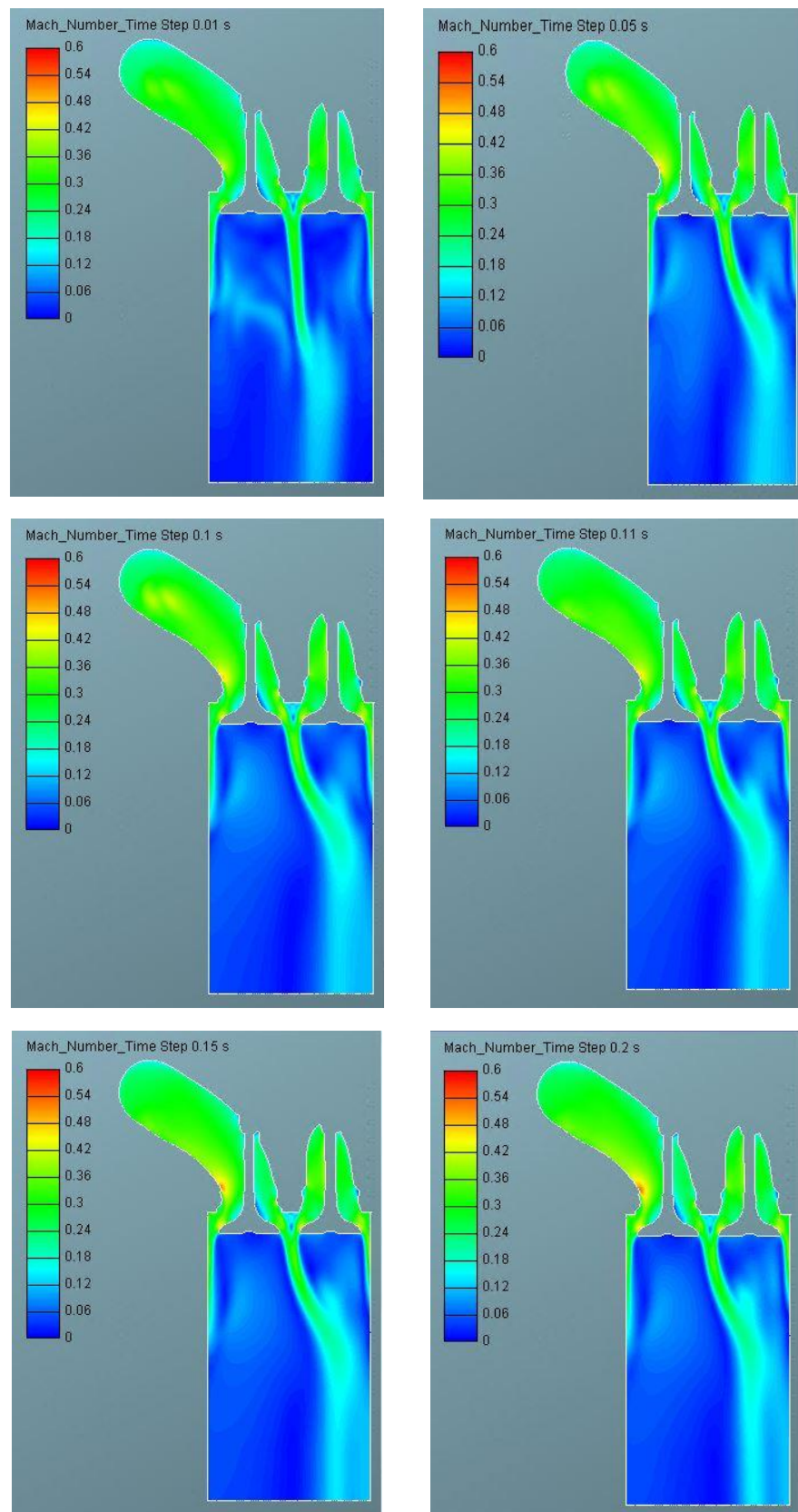


Figure 6.2:5 Mach Number of flows inside the cylinder for different time steps in seconds

The flow inside the cylinder is subsonic as the maximum Mach number inside the cylinder is around 0.4 near the valve, hence a good volumetric efficiency can be expected. Generally, volumetric efficiency tends to decrease if the Mach number exceeds the value of 0.6 [8].

The Mach number in of one intake port from the side view is shown in Figure 6.2:6

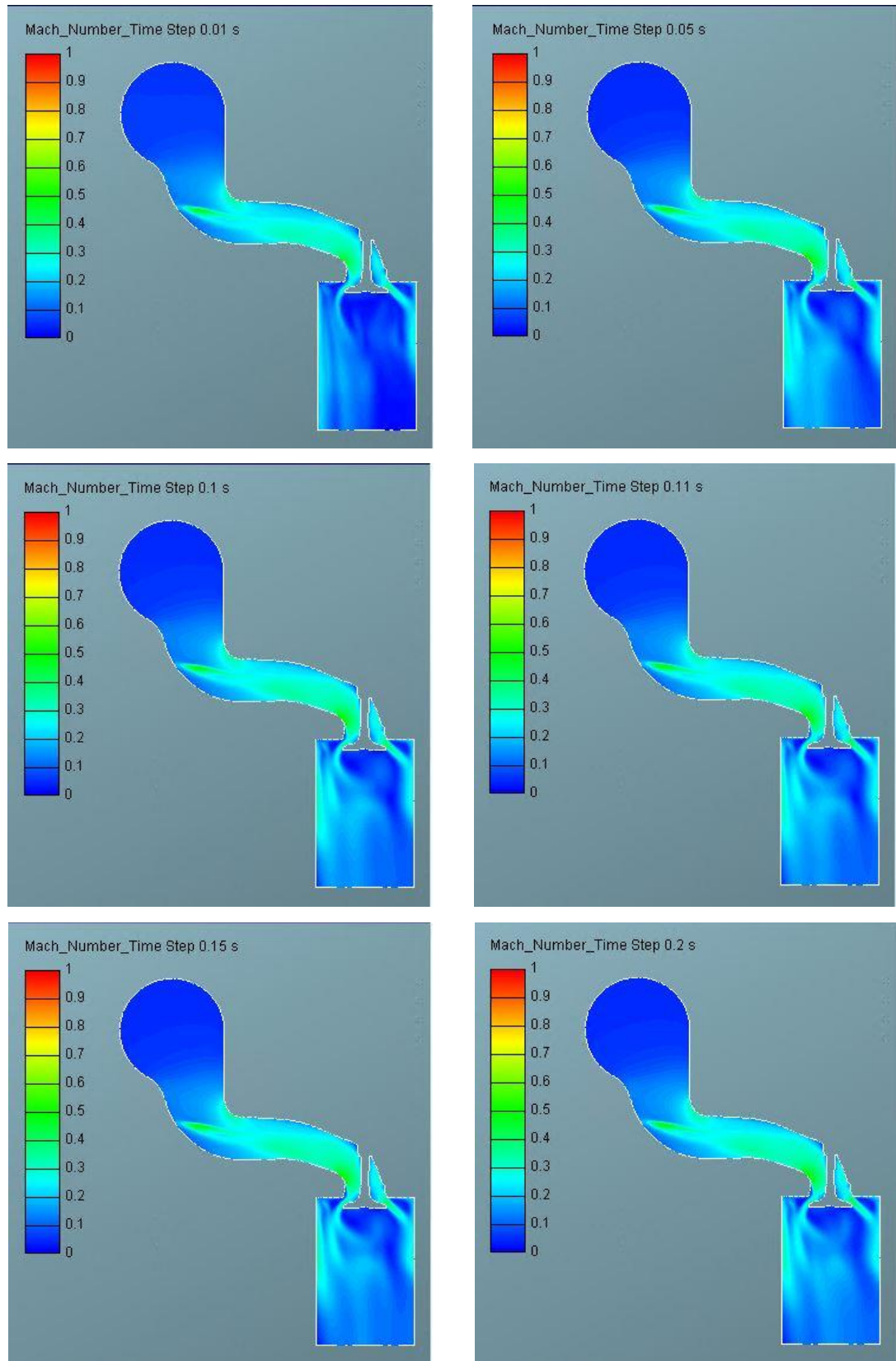


Figure 6.2:6 Mach number for one of the intake port from the side view and the start point of methane injection for different time steps in seconds.

The flow reaches a maximum value of about 0.6, hence there won't be high -pressure wave propagation which might will interfere with the induction process as the flow is subsonic [8].

The Mach number for the flows in the manifold inserts is shown in Figure 6.2:7

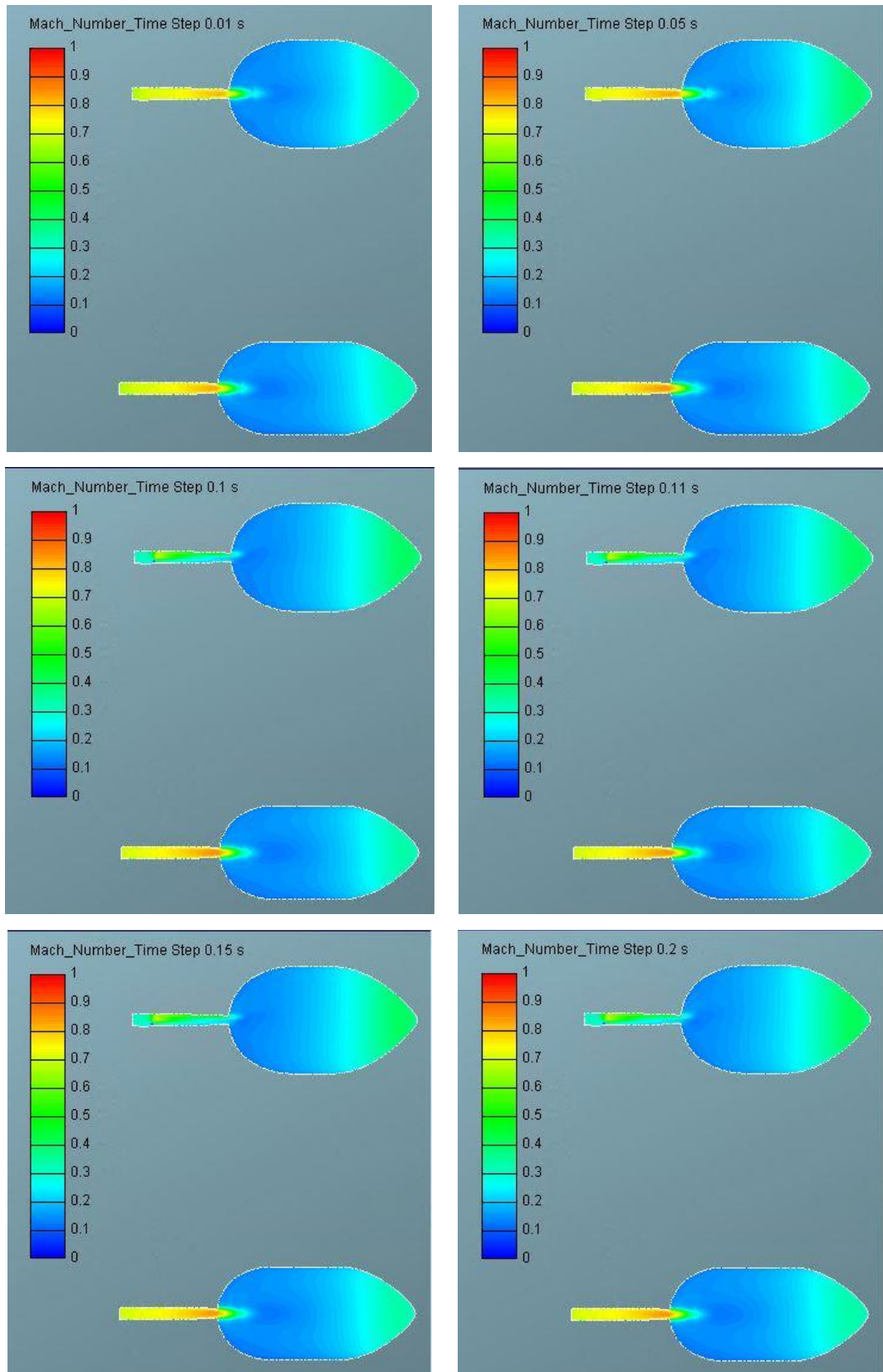


Figure 6.2:7 Mach Number of flows inside the cylinder for different time steps in seconds

The flow inside the manifold insert reaches a maximum value of about 0.9 near the exit, which is still subsonic, hence no choking of flow is expected which would interrupt the fuel flow to the intake ports. However, the fuel from the manifold inserts will expand inside the

intake ports which will reduce the fuel flow temperature from 293 K to a slightly lower temperature which can be seen in Figure 6.2:8.

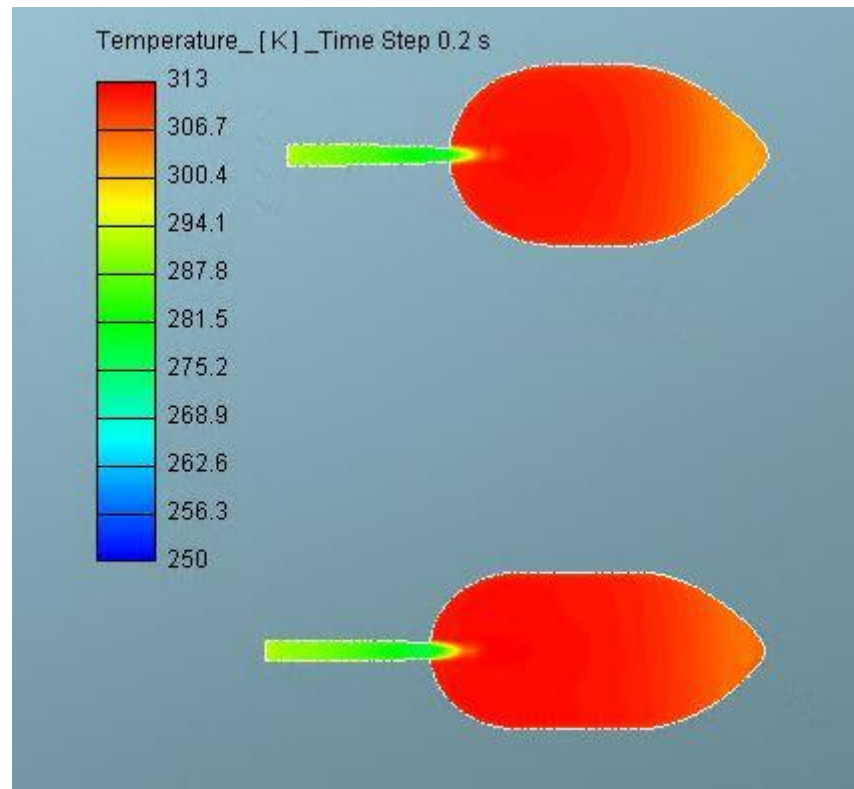


Figure 6.2:8 Temperature profile of manifold inserts

We can see in the figure above that the temperature at the inlet tip of the manifold inserts is about 294 K and then it gradually decreases as the flow processes towards the manifold outlet. The temperature at the outlet of manifold inserts is about 287 K where the fuel mixes with the air stream which is at temperature 313 K. This temperature drop is caused due to the expansion of the fuel jet into the intake ports.

7 Summary & Conclusion

This thesis deals with the conversion of an already existing diesel engine into a spark ignited gas engine. In Section 1 we have acquainted our self which the benefits of CNG as an alternative fuel for diesel & petrol operated engines. Also, we have seen why this conversion of a diesel engine is necessary to a SI GNG engine from an energy content point of view which would also result in lower emission.

The thesis was divided into two parts, where the primary goal is to convert an existing diesel engine into a SI gas engine. The design changes made and components selected for the conversion and the port fuel injection control strategy for methane as fuel have been discussed in Section 3, whereas the implementation of the design changes and the fuel injection control is discussed in Section 4 & 5. The CAD tool CREO was used for the parts, assembly, and detailed drawing preparation. The fuel injection parameters and strategy have been discussed in Section 4

The secondary goal of this thesis is to create and test a 3-D CFD model of an intake stroke with a predefined intake valve lift which gives a better understanding of air-fuel mixture development processes starting at the point of port injected fuel and continuing for the entire intake stroke in the cylinder. The model focuses on evaluating the mixture homogeneity of air & methane during an intake stroke. The simulation was done on the AVL FIRE™ software tool, which only deals with the steady-state condition, meaning that the intake valves and the piston were stationary.

Section 6 deals with the details of the simulation model setup. The simulation solver was set for mapping of several different parameters, but as this is the initial stage of the simulation observed the mass fraction of methane which would help to investigate the mixing of air-fuel, the flow velocities & Mach number to investigate if the flow was subsonic, sonic or supersonic.

Some key conclusions based on the component selection, design & fuel injection strategy are mentioned below.

- The pressure regulator of the Landi Renzo EVO model can be tuned up to 5 bars of absolute pressure, whereas the pressure regulator setting needed to maintain the required mass flow rate of fuel for the desired operating point is 4 bars of absolute pressure, therefore the selected model of the Landi Renzo Evo CNG kit will be sufficient to maintain the experimental engine at the given operating conditions which is 100 kW @ 2200 RPM.

- The user may tune the pressure regulator setting from 1 bar of absolute pressure up to 4.5 bars of absolute pressure if required. Based on the operating chart of the pressure regulator increasing the pressure above 4.5 bars will open the pressure relief valve inside the pressure regulator which will vent the fuel back to the tank.
- To maintain the experimental engine operating condition of 100 kW @ 2200 RPM it is necessary to have a fuel mass flow rate of 18 kg.h⁻¹ this means 4.5 kg.h⁻¹ per cylinder. But the intake valves are opened for a fraction of seconds, hence to get 4.5 kg.h⁻¹ fuel flow rate inside one cylinder it is necessary to maintain the actual fuel flow rate at 41.25 kg.h⁻¹ at each manifold insert at 4 bars absolute pressure inside the common rail.
- The fuel mass flow rate is extremely sensitive to the fuel injection time available. It was observed that increasing the injection time reduced the actual required mass flow rate of the fuel at the manifold inserts, hence it was decided to inject fuel for one complete engine cycle.
- Of all the intermediate connections from the common rail to the manifold inserts, the maximum fuel velocities are reached inside the manifold inserts which was 428 ms⁻¹ at 4 bars absolute pressure and 293 K fuel temperature, the velocity of sound for methane is 450 ms⁻¹ for these pressure and temperature conditions. The Mach number was calculated to be 0.9, this means that the flow inside the manifold inserts is still subsonic.

Some key conclusions based on the observations from AVL FIRE™ simulations are mentioned below.

- We can observe that the methane gas has the tendency to follow the curvature of the intake ports, this is caused because of the Coanda effect. A more suitable position for the manifold insert's ports can be near to the inlet valves where the fuel will be injected near the intake valve seats or near the intake valve head.
- We observed the air-fuel mixture development inside intake ports, near the valve head and inside the cylinder with a reference mass fraction value of methane as 0.058 corresponding to lambda 1. From the section views, we can see some places inside the intake ports show a diffusive type of mixing behavior whereas the mass fraction inside the cylinder varies from 0.0348 to 0.058 for the air-fuel mixture. Keeping these values as reference points we can now continue for a dynamic meshed model for more comprehensive analysis.

- The temperature at the inlet tip of the manifold inserts was observed at 294 K and then it gradually decreases as the flow processes towards the manifold outlet, where the temperature at the outlet of manifold inserts is about 287 K. This temperature drop is caused due to the expansion of the fuel jet into the intake ports.
- Flow inside the entire domain is subsonic based on the Mach number observed, hence we can expect good overall volumetric efficiency as the choking of flow will not occur inside the manifold insert's ports, inside the intake ports, and near the inlet valves.

8 Thesis Contribution & Future Research Scope.

Contribution of this thesis:

- Component selection with Manufacturer name, model name, and quantity to assemble fuel injection module for a 4-cylinder engine.
- 3-D model of all the necessary components along with technical drawings for manufacturing and assembly of the modules which can be used for CFD analysis of flow development if needed in the future.
- Pressure regulator setting & tuning calculation with all the necessary parameters to control the fuel mass flow rate which can be changed if needed in the future.
- AVL FIRE™ non-dynamic mesh files for single cylinder CFD analysis of the flow development simulations which can be changed if needed in the future.
- AVL FIRE™ Workflow Manager solver steering file (.SSF) with all the boundary conditions and initial conditions for single cylinder CFD analysis of the flow development simulations which can be changed if needed in the future.
- Design of all components needed for changeover of the exiting experimental diesel engine to a spark ignited diesel engine which can be taken as a reference for future changes.
- Reference data for the fuel injection strategy, mass fraction of methane & Mach numbers which will be useful for future optimization.

Future Research Scope

- The current CFD simulation has been performed with a non-dynamic single-cylinder mesh with fixed valve lifts and piston position which only simulates the intake stroke. A dynamic mesh model can be created to simulate the moving valves and piston which can also simulate the intake and the compression stroke to get a better idea of the air-fuel mixture.
- Full transient simulation of one complete engine cycle should be done to check the effect of the cycle to cycle variation and also the cylinder to cylinder variation as the fuel mixture is prepared inside the intake ports.
- A simulation model for part load engine operation & full load engine operation can be created using GT Suite and other 1 D CFD simulation software and the results of these simulations should be compared with the actual engine testing data.
- Open & close loop fuel injection control algorithms must be designed and integrated into the ECU to start the engine to have steady engine operation for data acquisition.

9 References

- [1] R. E. Rossman, "The Effect of Vehicular Emissions on Human Health," 2020. [Online]. Available: https://teachers.yale.edu/curriculum/viewer/initiative_08.07.09_u.
- [2] U. S. E. Protection, "Global Greenhouse Gas Emissions Data," 2018. [Online]. Available: <https://www.epa.gov/ghgemissions/global-greenhouse-gas-emissions-data>.
- [3] C. European, "Road transport: Reducing CO2 emissions from vehicles," 2020. [Online]. Available: https://ec.europa.eu/clima/policies/transport/vehicles/cars_en.
- [4] C. P. V. Manufacturing, "Compressed Natural Gas CNG as Alternative Fuel," 2018. [Online]. Available: <https://www.cpvmsg.com/news/cng-as-alternative-fuel/>.
- [5] A. V. D. C. Jr., "Natural gas and other alternative fuels for transportation purposes," *ScienceDirect*, vol. 10, no. 2, pp. 187-192, 2003.
- [6] J. Andres, "Scavenged Pre-chamber for a Light-Duty Truck Gas Engine," Diploma Thesis: Department of Automotive, Combustion Engine and Railway Engineering, Czech Technical University, Prague, 2016.
- [7] J. Vavra, M. Takats and V. K. a. M. Skarohlid, "Influence of Natural Gas Composition on Turbocharged Stoichiometric SI Engine Performance," *SAE International*, no. ISSN: 0148-7191, 2012.
- [8] J. Haywood, "Internal Combustion Engine Fundamentals", USA: McGraw-Hill, New York, ISBN 0-07-028637-X, 1988.
- [9] A. Kamane, "Gaseous Fuel Injection For Engine With A Scavenged Pre-Chamber," Diploma Thesis: Department of Automotive, Combustion Engine and Railway Engineering, Czech Technical University, Prague, 2019.
- [10] N. Nithyanandham, "Gaseous Fuel Injection For Engine With A Scavenged Pre-Chamber," Diploma Thesis: Department of Automotive, Combustion Engine and Railway Engineering, Czech Technical University, Prague, 2018.
- [11] M. Perin and T. Okoniewski, "Lean Burn Engines," *SAE International* , no. 2013-36-0402, 2013.
- [12] A.C.Alkidas, "Combustion-chamber crevices: The major source of engine-out hydrocarbon emissions under fully warmed conditions," *ScienceDirect*, vol. 25, no. 3, pp. 253-273, 1999.
- [13] H. R. Ricardo, "Internal Combustion Engine". USA Patent 1,27,942 , 9 July 1918.
- [14] W. Attard, "Turbulent Jet Ignition Pre-Chamber Combustion System For Spark Ignition Engines". Patent 13/286,638 , 3 May 2012.

- [15] W. Attard and P. Parsons, "Flame Kernel Development for a Spark Initiated Pre-Chamber Combustion System Capable of High Load, High Efficiency and Near Zero NOx Emissions.," *SAE International*, no. 2010-01-2260, 2010.
- [16] M. Ferrera, "Highly Efficient Natural Gas Engines," *SAE International*, no. 2017-24-0059, 2017.
- [17] M. Pardy, *Photon superluminal flow in the de Laval nozzle*, Brno: Masaryk University, Faculty of Science., 2014.
- [18] D. R. Bansal, "A Textbook of Fluid Mechanics and Hydraulica Machines.", New Delhi, India: Laxmi Publications Pvt. Ltd., 2010.
- [19] B. J. Cantwell, "Fundamentals of Compressible Flow", California: Department of Aeronautics and Astronautics, Standorf University., 2018.
- [20] J. Ferziger and M. Peric, *Computational Methods for Fluid Dynamics.*, 3 rd ed., Berlin; Heidelberg; New York; Barcelona;; Springer, 2002.
- [21] M. Jílek, *Thermomechanics*, Czech Technical University in Prague, 2006.
- [22] D. C. Wilcox, *Turbulence Modeling for CFD*, 3rd ed., California: Birmingham Press, Inc, 2006.
- [23] H. Versteeg and W. Malalasekra, *An Introduction to Computational Fluid Dynamics The Finite Volume Method*, 2nd ed., Harlow, England: Pearson Education, 2007.
- [24] M. Trancossi, "An Overview of Scientific and Technical Literature on Coanda Effect Applied to Nozzles," *SAE International*, no. 0148-7191, 2011.
- [25] A. Dumasa, M. Subhash, M. Trancossi and J. P. Marques, "The influence of surface temperature on Coanda effect," *Science Direct*, vol. 45, pp. 626-634, 2014.
- [26] *AVL Workflow Manager Documentation & User Manual*, Austria: Anstalt für Verbrennungskraftmaschinen List, 2019.
- [27] *AVL FIRE M Documentation & User Manual*, Austria: Anstalt für Verbrennungskraftmaschinen List, 2019.
- [28] K. Mahadevan and K. B. Reddy, *Design Data Handbook for Mechanical Engineers in SI and Metric Units*, 4th ed., CBS Publishers & Distributors, 2018.

List of Figure

Figure 1.1:1 Global Greenhouse Gas Emissions [2].....	4
Figure 2.1:1 Emission versus air/fuel ratio [9].	7
Figure 2.1:2 Schematic of flow processes by which piston crevice HC exit the cylinder: (a) exhaust blowdown process; (b) during exhaust stroke [12].....	8
Figure 2.2:1 Cross-section of a typical Pre-Chamber Combustion System [8]	10
Figure 2.2:2 Partial cross-section of Mahle Powertrain TJI system [14].....	10
Figure 2.2:3 Detailed cross-section of Mahle Powertrain TJI system [14].....	11
Figure 2.2:4 NO _x comparison of TJI and conventional SI engine [15].....	12
Figure 2.2:5 Normalised thermal efficiency comparison of TJI and conventional SI engine [15].....	12
Figure 3.2:1 Landi Renzo Evo Common Rail & Injectors	16
Figure 3.2:2 Landi Renzo Evo NG-1 Pressure Regulator.....	16
Figure 3.3:1 Schematic diagram for the CNG gas supply to the Landi Renzo Evo common rail.....	17
Figure 4.1:1 Schematic of the fuel flow through intermediate components for each cylinder.	20
Figure 4.1:2 Flow velocities of fuel across the intermediate connections with different pressure regulator settings.....	21
Figure 4.1:3 Pressure of fuel across the intermediate connections with different pressure regulator settings.....	23
Figure 4.2:1 Dependency of injection time available on fuel mass flow rate	26
Figure 5.1:1 Top view of the intake manifold with manifold insert holes drilled	28
Figure 5.1:2 Front sectional view of the intake manifold with manifold insert holes drilled .	28
Figure 5.1:3 The manifold inserts which will supply fuel inside the intake ports: (a) Cross-sectional view; (b) 3-D View.....	29
Figure 5.1:4 Front sectional view of the intake manifold with manifold insert assembly.....	29
Figure 5.2:1 Common rail holder with stud bolt assembly.....	30
Figure 5.2:2 Common rail with integrated injectors and holder assembly.....	30
Figure 5.2:3 Front view of common rail with integrated injectors and holder assembly	31
Figure 5.2:4 Top view common rail with integrated injectors and holder assembly	31
Figure 5.3:1 Intake Manifold, Manifold Inserts & Holder Assembly	32
Figure 5.3:2 Intake Manifold, Manifold Inserts, Holder & Common Rail with integrated Injectors Assembly.....	32
Figure 5.3:3 Complete Module Assembly	33

Figure 5.4:1 GWPB Flexible Gas Hose.....	34
Figure 5.4:2 Hose Clamps.....	34
Figure 5.4:3 Tee Split.....	35
Figure 6.1:1 Volumetric Mesh with grid.....	42
Figure 6.1:2 The intake ports, methane inlet ports (manifold inserts) and the cylinder detailed meshing grid	43
Figure 6.2:1 CH ₄ Mass Fraction Mapping for different time steps in seconds.....	45
Figure 6.2:2 Mass fraction mapping for one of the intake port from the side view and the start point of methane injection for different time steps in seconds.....	46
Figure 6.2:3 CH ₄ Mass Fraction Mapping for manifold inserts for different time steps in seconds.....	47
Figure 6.2:4 CH ₄ Mass Fraction Mapping for the top layer -10mm, middle layer -50mm and bottom layer -100mm from the cylinder head for different time steps in seconds.	48
Figure 6.2:5 Mach Number of flows inside the cylinder for different time steps in seconds .	49
Figure 6.2:6 Mach number for one of the intake port from the side view and the start point of methane injection for different time steps in seconds.	50
Figure 6.2:7 Mach Number of flows inside the cylinder for different time steps in seconds .	51
Figure 6.2:8 Temperature profile of manifold inserts	52

List of Tables

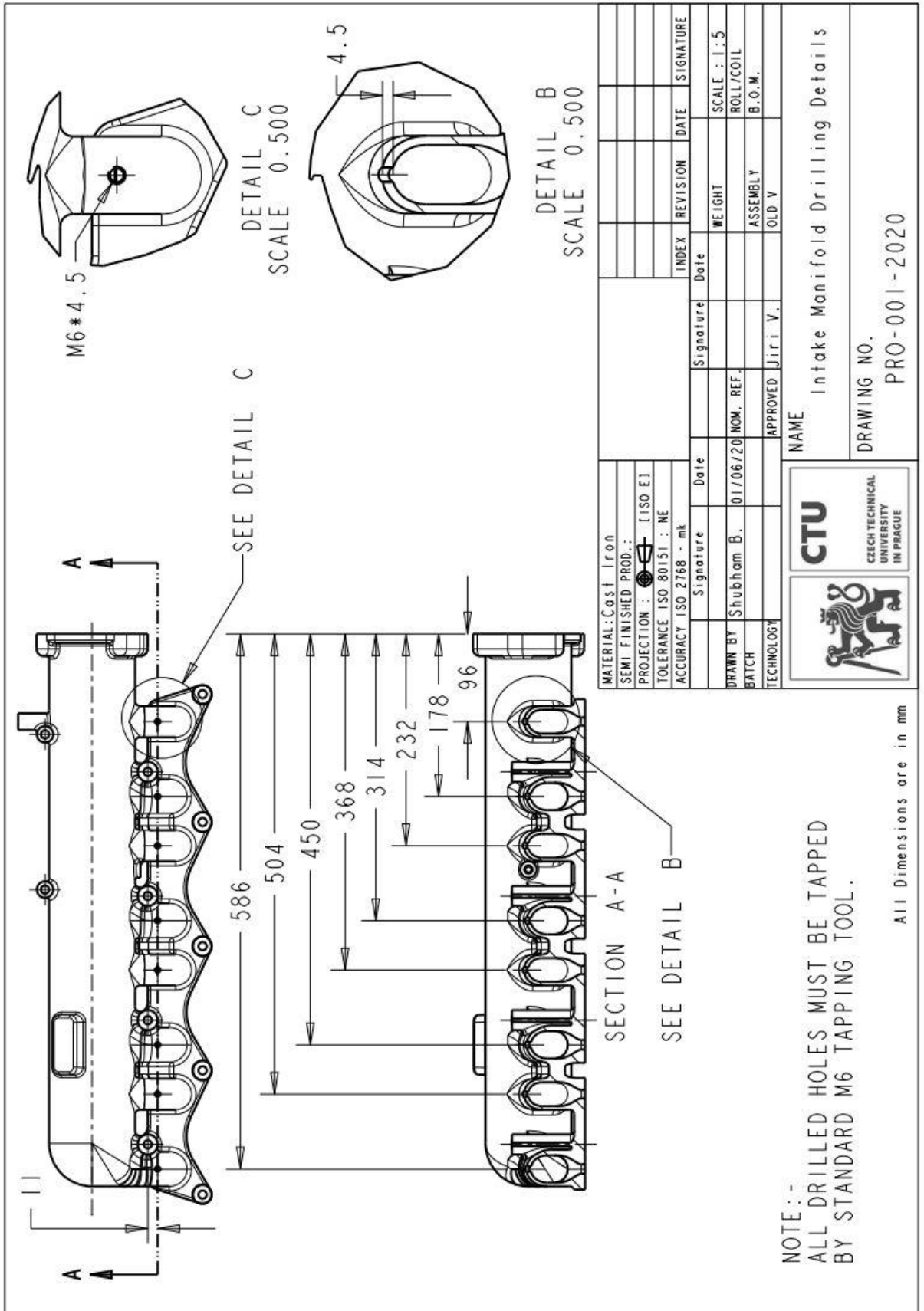
Table 3.1-1 Main parameter of the original engine arrangement.....	15
Table 3.2-1 Landi Renzo Evo Common Rail & Injector Parameters.	15
Table 3.2-2 Landi Renzo Evo Pressure Regulator Parameters.....	16
Table 4.1-1 Area of the elements in intermediate connections.	19
Table 4.1-2 Values of velocities for the intermediate connections for different pressure setting from the pressure regulator.....	20
Table 4.1-3 Methane density, specific heats & specific heat ratio.....	22
Table 4.1-4 Values of pressure for the intermediate connections for different pressure setting from the pressure regulator.....	22
Table 4.1-5 Intake Manifold & Intake Port pressure calculations.....	23
Table 4.1-6 Pressure drop across the inlet valve and effective pressure inside intake ports ..	23
Table 4.1-7 Exit Velocities & Mass flow rate of fuel according to Saint Venant & Wantzel equation.....	24
Table 4.2-1 Dependency of injection time available on fuel mass flow rate	25
Table 5.4-1 List of purchased material & suppliers.....	35
Table 6.1-1 Solver Steering File inputs & assumptions	43
Table 6.1-2 SSF Inputs for the boundary conditions on the surface selection.	44

List of Files in Attached CD

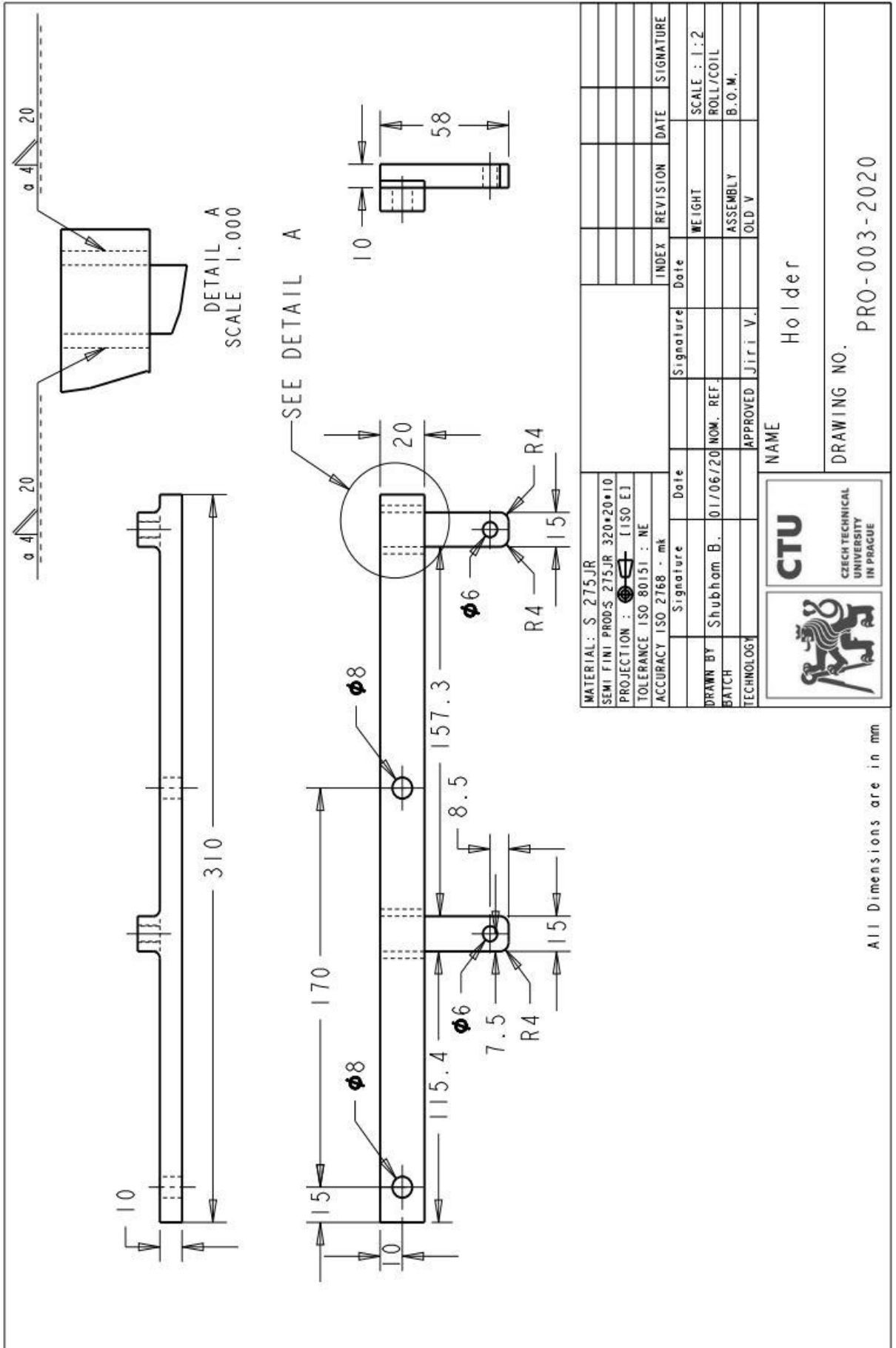
1. Diploma Thesis_Shubham Bawkar.pdf
2. AVL Fire workflow manager Solver Steering File. (Q-4_optSetting.ssf)
3. AVL Fire M 1-cylinder mesh file. (cfd_cyl_1.flm)
4. CAD Model
 - 4.1 Intake_Manifold.prt & .neu
 - 4.2 Holder.prt & .neu
 - 4.3 Landi_Renzo_Commonrail.prt & .neu
 - 4.4 Tee.prt & .neu
 - 4.5 Spipe (Hoses 1 to 4). prt & .neu
 - 4.6 Bend pipe (Hoses). prt & .neu
 - 4.7 Clamps.prt & .neu
 - 4.8 Manifold_inserts.prt & .neu
 - 4.9 Washer.prt & .neu
 - 4.10 M8_Nut.prt & .neu
 - 4.11 M6_Nut.prt & .neu
 - 4.12 Bolt_M6.prt & .neu
 - 4.13 Landi_Renzo_Rail.asm & .neu
5. Technical Drawings.pdf
6. Parts Purchase Details.xls

Attachments

Attachment A

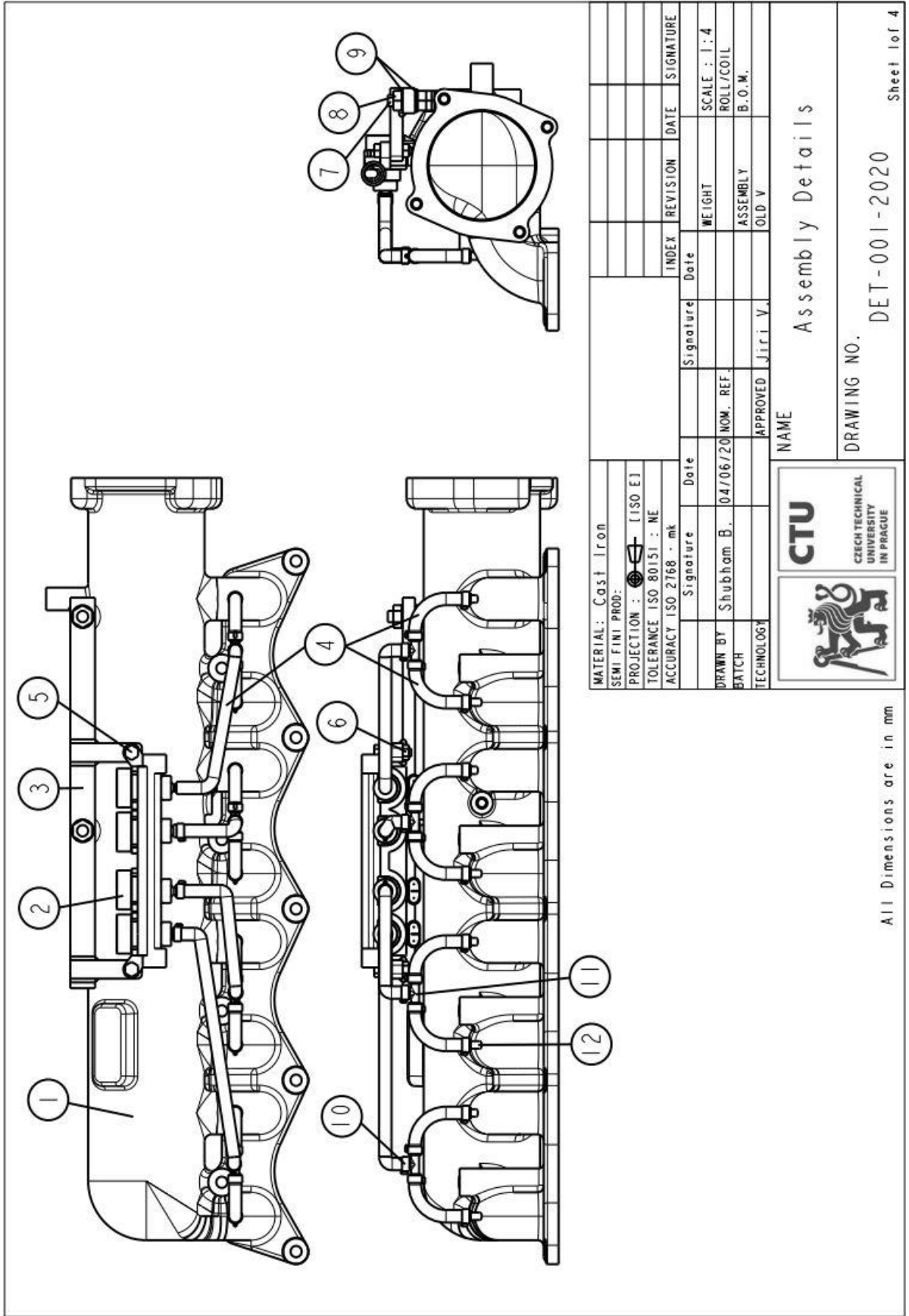


Attachment B

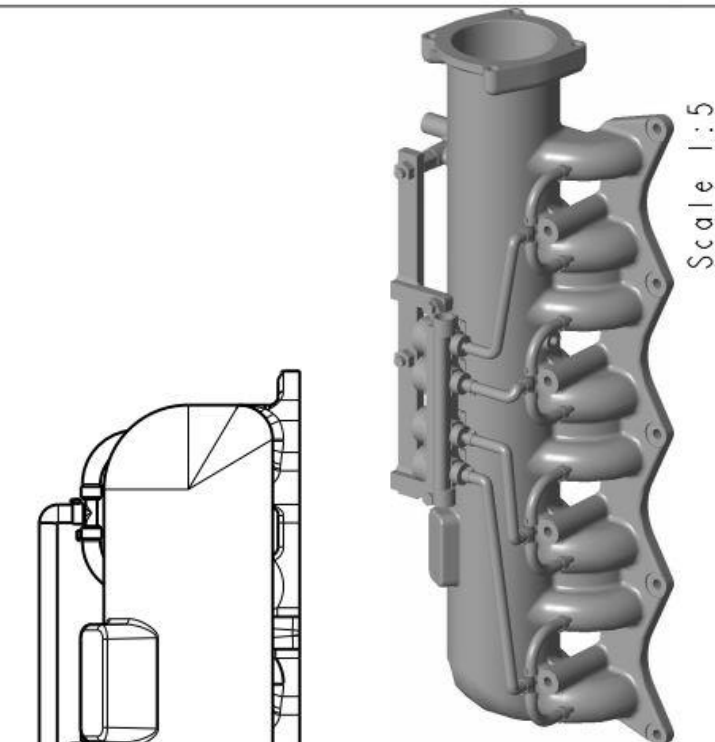


MATERIAL: S 275JR		Signature		Date	
SEMI FINI PRODS: 275JR 320*20*10		Shubham B.		01/06/20	
PROJECTION : (ISO E1)		NOM. REF.		SCALE : 1:2	
TOLERANCE ISO 80151 : NE		BATCH		ROLL/COIL	
ACCURACY ISO 2768 - mk		TECHNOLOGY		ASSEMBLY	
		APPROVED: Jiri V.		OLD V	
		NAME		Holder	
		DRAWING NO.		PRO-003-2020	

All Dimensions are in mm



All Dimensions are in mm



Scale 1:5

Note:-

- 1) The dimension 22.5 should be maintained by a spacer (hollow tube/ pipe) of the above given dimension.
- 2) All hoses connecting the common rail & Tee(4 Nos.) should be cut to length of 225 and then be assembled. (Assembly shows different lengths of hoses for asthetical purpose only).
- 3) All hoses connecting Tee & manifold insert (8 Nos.) should be cut to length of 40 and then be assembled.

MATERIAL: Cast Iron							
SEMI FINI PROD:  [ISO E1]							
PROJECTION :  [ISO E1]							
TOLERANCE ISO 80151 : NE							
ACCURACY ISO 2768 - mk							
Signature	Date	Signature	Date	Signature	Date	Signature	Date
Shubham B.	04/06/20						
DRAWN BY		NOM. REF.		WEIGHT		SCALE : 1:4	
BATCH				ASSEMBLY		ROLL/COIL	
TECHNOLOGY				OLD V		B.O.M.	
		APPROVED Jiri V.					
NAME				Assembly Details			
DRAWING NO.				DET-002-2020			



CTU

CZECH TECHNICAL UNIVERSITY IN PRAGUE

All Dimensions are in mm

Sheet 2 of 4

SECTION A-A

DETAIL B
SCALE 1:000

2	Manifold Insert	Landi Renzo (DET-001-2020)	Brass	8
1	Intake Manifold	Zetor (PRO-001-2020)	Cast Iron	1
Sr No	Part Name	Description	Material	Quantity

Note :-

- 1) Teflon tape must be used (min 5 turns) around the threads to seal & avoid gas leakage during operation.
- 2) All the manifold inserts must be fastened for atleast 4 - 5 threads

All Dimensions are in mm

MATERIAL: Cast Iron SEMI FINI PROD: PROJECTION : [ISO E] TOLERANCE ISO 80151 : NE ACCURACY ISO 2768 - mk	Signature _____ Date _____ Shubham B. 04/06/20 NOM. REF. BATCH _____ APPROVED Jiri V. _____ TECHNOLOGY _____	INDEX _____ REVISION _____ DATE _____ SIGNATURE _____ WEIGHT _____ SCALE : 1:5 ASSEMBLY _____ ROLL/COIL _____ OLD V _____ B.O.M. _____
NAME _____ Assembly Details		
DRAWING NO. DET-003-2020		

CTU
CZECH TECHNICAL UNIVERSITY IN PRAGUE

Sheet 3 of 4

12	Manifold Insert	Landi Renzo	Brass	8
11	Tee	TRS 4-6-4 (693046)	-	4
10	Hose Clamp 12-22*9	DIN 3017 (680012)	EN 10142	24
9	Washer M8*1.8	DIN 125	EN 1,4401	12
8	Nut M8*6.8	DIN 934	EN 1,4401	8
7	Stud M8*70	DIN 931	EN 1,4401	2
6	Nut M6*5.2	DIN 934	EN 1,4401	2
5	Bolt M6*25	DIN 931	EN 1,4401	2
4	Flexible Hose	GWPB Hose	EN 559:2003	12
3	Holder	S275JR(PRO-003-2020)	EN 10025	1
2	Commonrail	Landi Renzo Evo	Plastic	1
1	Intake Manifold	Zetor(PRO-001-2020)	Cast Iron	1
Sr No.	Part Name	Description/ Norm	Material	Quantity

MATERIAL :					
SEMI FINI PROD:					
PROJECTION :	 1:ISO E1				
TOLERANCE ISO 80151 :	NE				
ACCURACY ISO 2768 :	mk				
Signature	Date	Signature	Date	INDEX	REVISION
DRAWN BY	Shubham B.	04/06/20	NOM. REF.	WEIGHT	SCALE : - -
BATCH				ASSEMBLY	ROLL/COIL
TECHNOLOGY				OLD V	B.O.M.
APPROVED		Jiri V.			
NAME		Bill Of Materials.			
DRAWING NO.		DET-004-2020			



All Dimensions are in mm